NASA TECHNICAL NOTE

NASA TN D-8466

FACTORS AFFECTING ION KINETIC TEMPERATURE, NUMBER DENSITY, AND CONTAINMENT TIME IN THE NASA LEWIS BUMPY-TORUS PLASMA

J. Reece Roth

Lewis Research Center
Cleveland, Ohio 44135

NATIONAL AERONAUTICS AND SPACE ADMINISTRATION • WASHINGTON, D. C. • MAY 1977

1. Report No.	2. Government Accession No.	3. Recipient's Catalog No.
NASA TN D-8466		

4. Title and Subtitle	5. Report Date
FACTORS AFFECTING ION KINETIC TEMPERATURE, NUMBER DENSITY, AND CONTAINMENT TIME IN THE NASA LEWIS BUMPY-TORUS PLASMA	May 1977
	6. Performing Organization Code
7. Author(s)	8. Performing Organization Report No.
J. Reece Roth	E-9042
	10. Work Unit No.
9. Performing Organization Name and Address	506-25
Lewis Research Center National Aeronautics and Space Administration Cleveland, Ohio 44135	11. Contract or Grant No.
	13. Type of Report and Period Covered
12. Sponsoring Agency Name and Address	Technical Note
National Aeronautics and Space Administration Washington, D.C. 20546	14. Sponsoring Agency Code

15. Supplementary Notes

16. Abstract

The toroidal ring of plasma contained in the NASA Lewis bumpy-torus facility may be biased to positive or negative potentials approaching 50 kV by applying dc voltages of the respective polarity to 12 or fewer midplane electrode rings. The electric fields, which are responsible for raising the ions to high energies by $E \times B/B^2$ drift, then point radially outward or inward. In this report, factors that affect the ion kinetic temperature, number density, and containment time in the plasma are given. These factors include the degree of toroidal symmetry of the plasma, the number of midplane electrode rings, the configuration of electrode rings, and the location of the diagnostic instruments with respect to the electrode rings used to generate the plasma. Impurities were deliberately introduced into the plasma, and the effects of the impurity fraction on ion kinetic temperature and electron number density were observed. It is concluded that, if necessary precautions are taken, the plasma communicates extremely well along the magnetic field lines and displays a high degree of symmetry from sector to sector for a wide range of electrode ring configurations and operating conditions. Finally, some characteristic data taken under nonoptimized conditions are presented, which include the highest electron number density (2.7×10^{11} particles/cm^3 on axis) and the longest particle containment time (1.9 msec) observed so far in this experiment. Also, evidence from a paired comparison test is presented which shows that the electric field acting along the minor radius of the toroidal plasma improves the plasma density and the calculated containment time more than an order of magnitude if the electric field points inward, relative to the values observed when it points (and pushes ions) radially outward.

17. Key Words (Suggested by Author(s))	18. Distribution Statement
Diocotron instability; Toroidal confinement; Plasma control; Electric fields; Bumpy torus; Radial transport	Unclassified - unlimited STAR category 75

19. Security Classif. (of this report)	20. Security Classif. (of this page)	21. No. of Pages	22. Price*
Unclassified	Unclassified	65	A04

* For sale by the National Technical Information Service, Springfield, Virginia 22161

CONTENTS

FACTORS AFFECTING ION KINETIC TEMPERATURE, NUMBER DENSITY, AND CONTAINMENT TIME IN THE NASA LEWIS BUMPY-TORUS PLASMA

by J. Reece Roth

Lewis Research Center

SUMMARY

The toroidal ring of plasma contained in the NASA Lewis bumpy-torus facility may be biased to positive or negative potentials approaching 50 kilovolts by applying direct-current voltages of the respective polarity to 12 or fewer midplane electrode rings. The electric fields, which are responsible for raising the ions to high energies by $E \times B/B^2$ drift, then point radially outward or inward. In this report, factors that affect the ion kinetic temperature, number density, and containment time in the plasma are given. These factors include the degree of toroidal symmetry of the plasma, the number of midplane electrode rings, the configuration of the electrode rings, and the location of the diagnostic instruments with respect to the electrode rings used to generate the plasma. Impurities were deliberately introduced into the plasma, and the effects of the impurity fraction on ion kinetic temperature and electron number density were observed. It is concluded that, if necessary precautions are taken, the plasma communicates extremely well along the magnetic field lines and displays a high degree of symmetry from sector to sector for a wide range of electrode ring configurations and operating conditions. Finally, some characteristic data taken under nonoptimized conditions are presented, which include the highest electron number density (2.7×10^{11} particles/cm^3 on axis) and the longest particle containment time (1.9 msec) observed so far in this experiment. Also, evidence from a paired comparison test is presented which shows that the electric field acting along the minor radius of the toroidal plasma improves the plasma density and the calculated containment time more than an order of magnitude if the electric field points inward, relative to the values observed when it points (and pushes ions) radially outward.

INTRODUCTION

The steady-state plasma in the NASA Lewis bumpy-torus facility is generated by a

modified Penning discharge operated in conjunction with the bumpy-torus magnetic field geometry. The origins and history of the basic bumpy-torus magnetic containment geometry have been reviewed in references 1 and 2. The combination of the modified Penning discharge with the bumpy-torus magnetic containment configuration was first proposed in 1967 (ref. 3). The characteristics and performance of the NASA Lewis superconducting bumpy-torus magnet facility have been described in references 4 to 6. The magnet array is shown in the isometric cutaway drawing in figure 1 and consists of 12 superconducting coils equally spaced around a toroidal volume 1.52 meters in major diameter. Each coil has a minor diameter of 19 centimeters, and the maximum designed magnetic field on the magnetic axis is 3.0 teslas. The minimum magnetic field on the magnetic axis between coils is 40 percent of the maximum magnetic field. The coil array is located in a single vacuum tank 2.6 meters in major diameter.

The bumpy-torus experiment at the NASA Lewis Research Center was preceded by approximately 9 years of research and development on a modified Penning discharge that was operated in a superconducting magnetic mirror facility. The ion heating mechanism associated with the modified Penning discharge was experimentally explored, and a consistent model was developed to describe it (refs. 7 to 10).

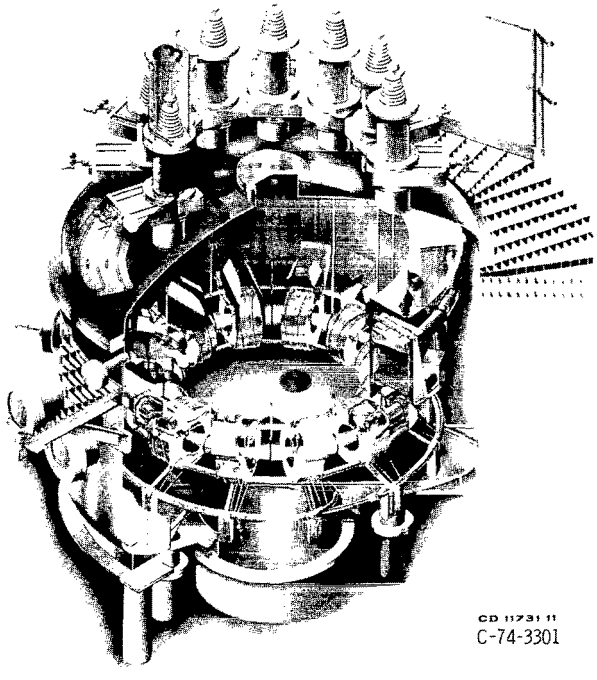

Figure 1. - Isometric cutaway drawing of NASA Lewis bumpy-torus magnet facility.

The bumpy-torus plasma is shown in figure 2, which was taken through one of the 25-centimeter-diameter glass viewports in the equatorial plane of the torus. The vertical element in the foreground is the near side of an 18-centimeter-inside-diameter, water-cooled anode ring located at the midplane of the plasma, which is maintained at positive direct-current potentials up to 50 kilovolts. Visible to the left of center in the background are the anode ring and the plasma at the opposite diameter of the toroidal array. The plasma floats at a high positive potential when a positive voltage is applied to the circular midplane electrode rings.

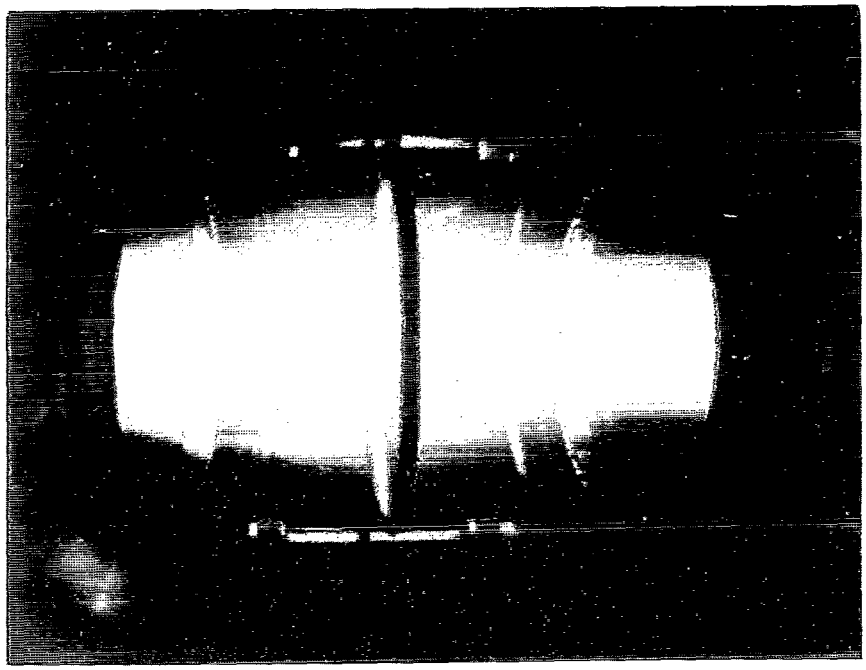

Figure 2. - Bumpy-torus plasma viewed along equatorial plane of torus. (The plasma at opposite diameter of torus is visible to left of the electrode ring in the foreground.)

The NASA Lewis bumpy-torus experiment possesses four distinguishing characteristics:

(1) The plasma, the magnetic field, and the ion heating mechanism are operated in the steady state.

(2) The ion kinetic temperature is typically more than a factor of 10 higher than the electron temperature.

(3) The plasma is acted on by a combination of strong direct-current magnetic and electric fields.

(4) The necessary fusion technology is being developed in parallel with the physics, particularly superconducting magnet technology and cryogenic, vacuum, and high-voltage techniques.

The presence of strong radial electric fields acting on the plasma, which usually exceed 1 kV/cm, not only is responsible for raising the ions to energies of the order of kilovolts, but also affects the containment of the plasma. Previous investigations (refs. 1, 2, 11, and 12) have shown that, in common with Penning discharges and magnetron-like devices, the plasma forms rotating spokes that gyrate around the minor circumference of the plasma with velocities comparable to the E/B drift velocity. The ions of these rotating spokes then form an energy reservoir that is thermalized to the high kinetic temperatures observed. As is shown later in this report, the strong radial electric fields also have a profound effect on the radial transport and containment of the plasma.

The only other active experiment using the bumpy-torus containment geometry is the ELMO bumpy-torus experiment at the Oak Ridge National Laboratory, where Dandl and coworkers (refs. 13 to 15) have carried out experimental investigations on electron cyclotron resonance heating. The approach taken in the NASA Lewis bumpy-torus experiment differs from the ELMO experiment in that the latter creates a stable magnetic well in each sector of the torus with high-beta hot electrons, which are generated by absorption of radiofrequency power, and the ion population is heated by binary collisions with the more energetic electrons. In the Lewis bumpy torus, direct-current electric fields are applied to the plasma by external electrodes, and the ion population is directly raised to high energies by E/B drift. This results, after thermalization, in ion kinetic temperatures more than a factor of 10 higher than the temperature of the electron population.

The work described in the following two sections of this report was required to lay the groundwork for the measurement of the average plasma number density by a microwave interferometer using a novel polarization diplexing technique, and also to document the assumptions and procedures used to measure both the particle and energy containment times in the NASA Lewis bumpy-torus plasma. It has been observed in previous work (refs. 1 and 16) that the particle number density and containment time depend on the number of midplane electrode rings, with the containment time and number density being highest when three anode rings were used to generate the plasma. Before this and other factors could be optimized, it became necessary to distinguish between the effects of varying the number of midplane electrode rings, the radial position of the electrode rings, or the value of a weak vertical magnetic field and the effects due to asymmetries of the toroidal plasma or to a systematic dependence on the relative configuration of the electrode rings and the diagnostic instruments. Measurements are reported on the degree of symmetry of the toroidal plasma and of the effects of electrode ring configuration on the ion number density and kinetic temperature.

The impurities normally present in the bumpy torus amount to 1 percent or less of the background deuterium pressure at which the plasma is operated. Controlled

amounts of impurity gases were deliberately introduced into the plasma. The ion kinetic temperature, the nature of the ion energy distribution function, and the electron number density were observed as the impurity concentrations were varied.

DENSITY MEASUREMENT WITH POLARIZATION DIPLEXING MICROWAVE INTERFEROMETER

Steady-state operation of the bumpy-torus plasma, combined with the high power (up to 150 kW) dissipated in the plasma, results in heating of the microwave hardware and thermal expansion effects, which make the data from conventional microwave interferometry unreliable and/or difficult to interpret. To overcome the special diagnostic problems of the bumpy-torus plasma, a novel microwave interferometer based on polarization diplexing was developed at the NASA Lewis Research Center with the assistance of Professor Andrew L. Gardner of Brigham Young University under NASA university grant NSG-3068. The principles of operation of this interferometer and its performance characteristics are described in references 17 to 19. Briefly, both the ordinary and extraordinary waves are propagated through the plasma and reflected from a spherical reflector back into the square microwave horn from which they were launched. It can be shown that the integrated electron number density is proportional to the phase angle between the two modes of propagation. Since the two modes of propagation are affected equally by thermal expansion effects, the sensitivity and stability of the density measurement are unaffected by such thermal effects.

Interferometer Location

An isometric cutaway drawing of the interferometer in the vacuum tank is shown in figure 3. The axis of the interferometer was located as close as possible to the magnetic field coil in order to avoid reflections from the midplane electrode ring and also because the extraordinary mode will not propagate through the plasma at weak magnetic fields.

Figures 4 and 5 show a scale drawing of the interferometer location with respect to the magnetic field coil windings and spoolpiece. Contour lines of equal magnetic field strength are shown in the working volume. Figure 4 is a plan view of the interferometer location in the equatorial plane of the torus, and figure 5 is an elevation on a cylindrical surface, the radius of which is equal to the geometric radius of the toroidal array (76 cm). To relate the plasma number density to the phase change of the extraordinary

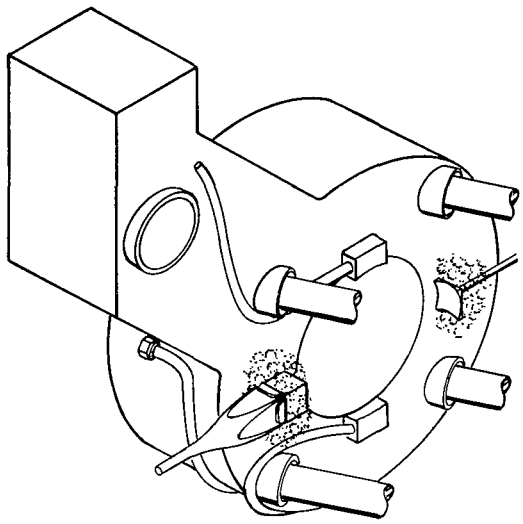

CD-12027-75

Figure 3. - Isometric cutaway drawing showing location of microwave interferometer in sector 10. (The axis of the interferometer is in the equatorial plane of the torus, with a square reflecting mirror inside the plasma and a square microwave horn outside.)

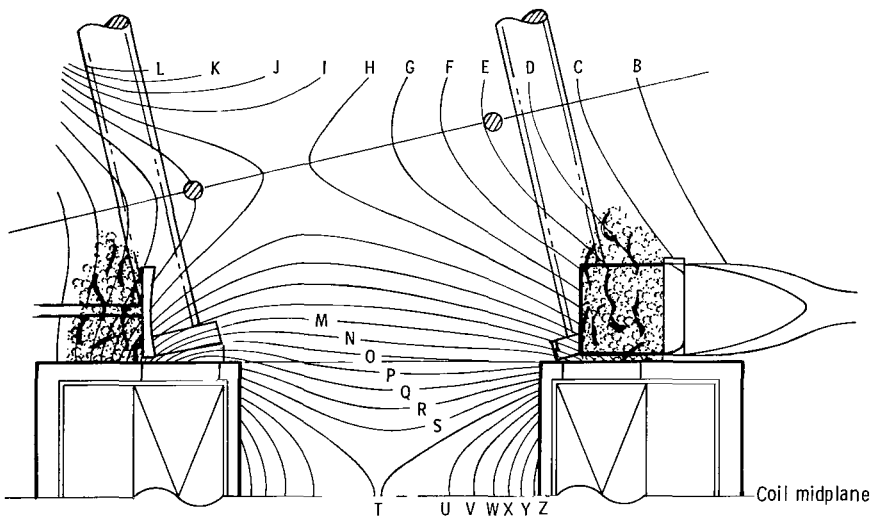

CD-12024-75

Contour	Normalized magnetic field strength
A	0.050
B	.100
C	.150
D	.200
E	.250
F	.300
G	.350
H	.400
I	.450
J	.500
K	.550
L	.600
M	.650
N	.700
O	.750
P	.800
Q	.850
R	.900
S	.950
T	1.000
U	1.050
V	1.100
W	1.150
X	1.200
Y	1.250
Z	1.300

Figure 4. - Location of microwave interferometer with respect to magnetic field, where contour lines of equal magnetic field strength are shown in a plan view in the equatorial plane of the torus.

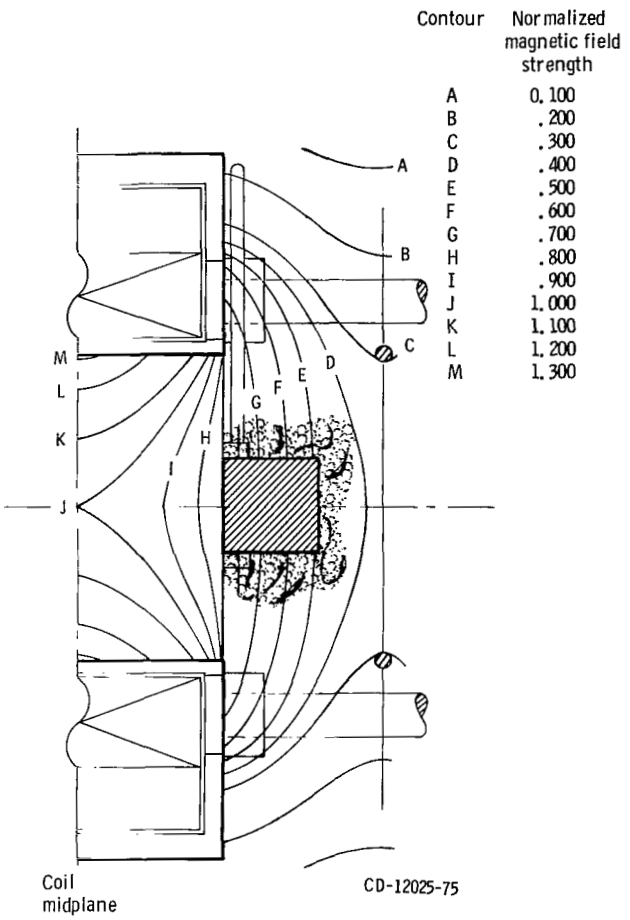

Figure 5. - Location of microwave interferometer with respect to magnetic field, viewed in elevation on a cylindrical surface, the radius of which is equal to the geometric major radius of the toroidal volume.

mode, we must know the magnetic field strength within the entire plasma volume. The magnetic field strength in the volume perceived by the interferometer beam was calculated from the same computer program that produced the contour profiles in figure 4.

Figure 6 shows a plan view of the interferometer location with respect to the electrode ring and the magnetic field lines, which tend to define the plasma boundary. The plasma confined in the bumpy torus has axial as well as radial density gradients, so it is somewhat more difficult to find a density that characterizes the entire plasma than it is in an axisymmetric plasma such as the Tokamak. The interferometer is located about halfway between the midplane and the magnetic mirror throat, so the average density across the diameter at that axial position should be roughly characteristic of the average of the entire plasma.

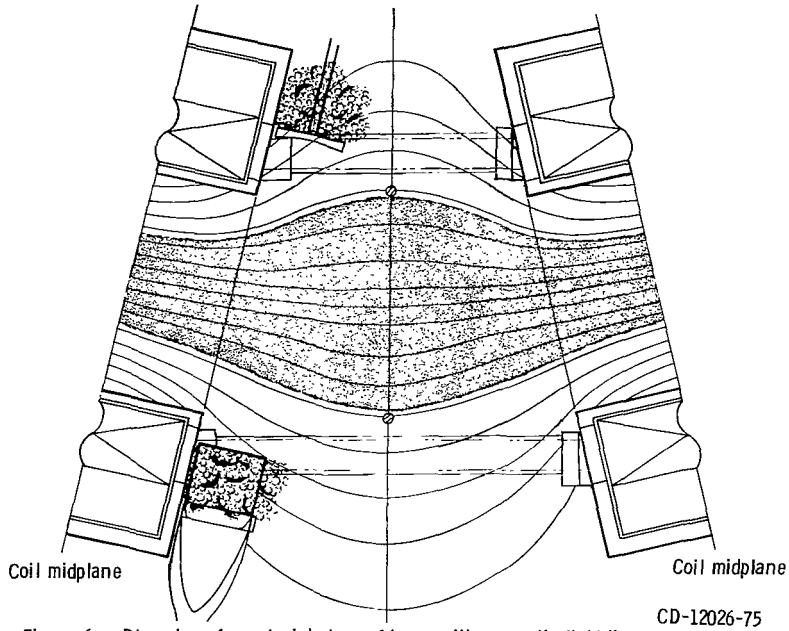

Figure 6. - Plan view of equatorial plane of torus with magnetic field lines and plasma boundaries indicated.

Spectroscopic Midplane Radial Number Density Profiles

Like all microwave interferometers, this instrument measures the integrated electron number density across the plasma diameter, so it is necessary to know the radial profile in order to estimate the maximum number density on the plasma axis. No radial profiles of electron number density have been measured at the axial position of the microwave interferometer. However, spectroscopic measurements of relative number density profiles have been made in the midplane by Richardson (refs. 1, 2, 16, and 20).

A characteristic number density profile in the high-pressure mode has been taken from reference 1 and is plotted in figure 7. The radial density profile that best fits the data is a linear falloff of electron number density with increasing radius. There is a small enhancement near the inner boundary of the anode ring, where the anode sheath exists. For this triangular density distribution, the average electron number density is one-half the maximum value on the plasma axis. Two characteristic profiles in the low-pressure mode of operation are shown in figure 8. The profile of relative number density is relatively flat in this mode of operation, with an enhancement near the anode sheath, where the ionization process is most active. Shown superimposed on these two density profiles is the profile corresponding to the same integrated electron number density across the plasma diameter. The outer boundary of these profiles is determined by

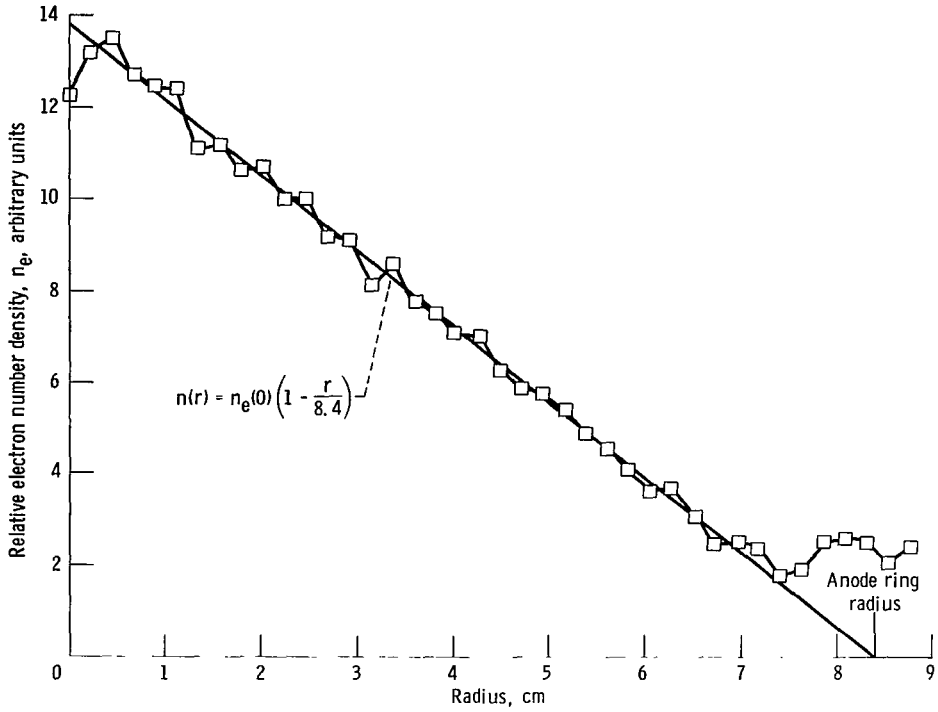

Figure 7. - Spectroscopically determined profiles of relative electron number densities across midplane of plasma in high-pressure mode. Background deuterium density, n_0, 8.6×10^{11} particles/cm^3 (26 μtorr); electrode voltage, V_a, 6.0 kilovolts; electrode current, I_a, 0.35 ampere; ion kinetic temperature, T_i, 460 electron volts.

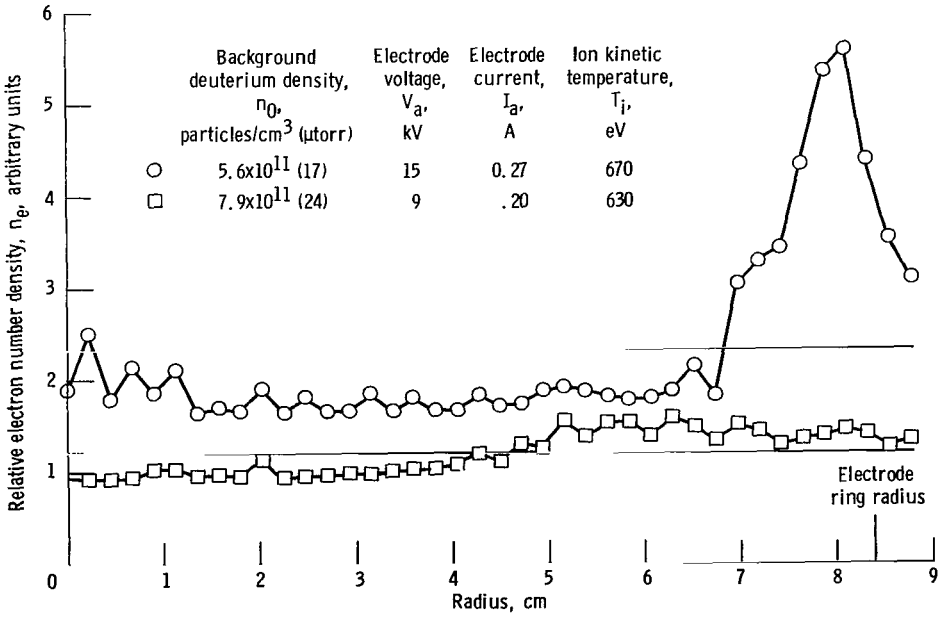

Figure 8. - Spectroscopically determined profiles of relative electron number densities across midplane of plasma in low-pressure mode.

the inner diameter of the midplane electrode rings. The diameter of the plasma was measured at the axial location of the microwave interferometer and found to be 13.2 centimeters. This is in good agreement with a projection along the magnetic field lines from the inner circumference of the midplane electrode rings. For positive electrode potentials, the triangular and flat distributions shown in figures 7 and 8 are characteristic of the relative number density profiles in the high- and low-pressure modes of operation, respectively (refs. 1, 2, 16, and 20), and were used as a basis for relating the microwave phase shift to the average and maximum electron number densities.

The relative number density profiles shown in figures 7 and 8 cannot result from diffusional radial transport processes that occur in plasmas confined by magnetic fields alone. Transport processes based on Fick's law of diffusion require that the radial density profile have a second derivative. The flat and triangular distribution functions shown in figures 7 and 8 do not possess a finite second derivative. These profiles suggest that the radial transport processes are profoundly modified by the presence of the radial electric field and that one cannot understand the radial transport in terms of a purely diffusive process incorporating Fick's law.

Relation of Phase Shift to Electron Number Density

The computations necessary to relate the angular phase shift to the electron number density in the plasma were performed in reference 19. The information required in this computation included the radial density profiles, which were based on figures 7 and 8; the value of the magnetic field at each point in the microwave beam; and the intensity profile of the microwave energy along the axis of the microwave interferometer between the horn and the reflector. The average electron number density is based on a 13.2-centimeter diameter. For the triangular density profile, the maximum density on the axis is higher by a factor of 2.

Both profiles in figures 7 and 8 yield a linear relation between phase angle and density up to densities approaching 10^{12} particles/cm^3. This relation greatly simplifies interpretation of the experimental data and comes about because nonlinear effects of the ordinary and extraordinary modes tend to cancel out. The sensitivity of the interferometer system is such that densities as low as 10^8 electrons/cm^3 can be measured.

CALCULATION OF PARTICLE AND ENERGY CONTAINMENT TIMES

Theoretical Analysis

Obtaining the particle and energy containment times for a confined plasma has been one of the most difficult diagnostic problems in controlled fusion research. The particle and energy containment times are usually obtained by a model-dependent procedure, in which the measured plasma properties are introduced into a computer model that includes a particle and energy balance of the plasma. A simple model relating the particle and energy containment times to direct plasma measurements is possible in the NASA Lewis bumpy-torus plasma. The plasma is subjected to strong electric fields, and it is reasonable to assume that the ions and electrons are lost to the respective electrodes. The percentage of ionization is less than 20 percent for data presented in this report. Volume recombination is negligible, and the plasma is not charge-exchange dominated (ref. 1, fig. 9(a)). The power supply voltage and current can be measured to 1-percent accuracy and, in combination with other measured plasma parameters, can yield the particle and energy containment times.

We assume that the average electron number density from the microwave interferometer is characteristic of the 82-liter volume of the bumpy-torus plasma, that particle flow to the electrodes is not ambipolar, and that any parasitic currents which flow outside the plasma volume between the electrodes and the ground are negligibly small. This latter assumption is discussed in the section Direct Measurement of Parasitic Power Flux. If these assumptions are valid, the relation between the electrode current to the power supply and the particle containment time may be written as follows:

$$I_p = \frac{e\bar{n}_e V_p}{\tau_c} \tag{1}$$

where I_p is the total current flowing to all of the electrode rings, V_p is the plasma volume, and τ_c is the average particle containment time. Equation (1) merely states that the current flowing to the power supply is equal to the average rate at which charge is lost from the plasma. We can rearrange equation (1) to obtain the particle containment time in terms of measured parameters as follows:

$$\tau_c = \frac{e\bar{n}_e V_p}{I_p} \tag{2}$$

Since the plasma volume is known, equation (2) states that the particle containment time

can be calculated from the average electron number density and the current flowing to the power supply.

The electron temperature is much less than the ion temperature in this plasma, so the power flowing to the plasma may be written as

$$W_p = \eta_i I_p V_a = \frac{\frac{3}{2}\bar{n}_e e V_p T_i}{\tau_E} \tag{3}$$

where η_i is the ion heating efficiency, the numerator of the right side is the energy density of the plasma, and the denominator is the energy containment time. The power flowing to the plasma is a product of the electrode current and the voltage in this steady-state experiment. We can obtain the energy containment time in terms of measured quantities as follows:

$$\tau_E = \frac{\frac{3}{2}\bar{n}_e e V_p T_i}{\eta_i I_p V_a} = \frac{3}{2}\frac{\tau_c}{\eta_i}\frac{T_i}{V_a} \tag{4}$$

Thus, we can measure the energy containment time of the bumpy-torus plasma by additionally measuring the ion kinetic temperature. Previous experimental investigations reported in reference 11 showed that the ratio of ion kinetic temperature to electrode voltage ranged from about 5 to 23 percent. The ratio of energy to particle containment times in this plasma would then range from about 1/13 to 1/3. It is clear from equations (2) and (4) that the calculation of the energy and particle containment times in the bumpy-torus plasma is a simple matter, once the average electron number density is known. The values obtained depend only on the assumptions that no parasitic currents flow between the electrodes outside the plasma volume and that particle flow to the electrodes is not ambipolar. These latter assumptions are addressed in the following sections.

Supportive Spectroscopic Data

One independent check on the proportionality of equation (2) was made with spectroscopic data, which are shown in figures 9 and 10. The relative electron number density averaged across a chord of the plasma was measured spectroscopically along with the average particle residence time (refs. 1, 2, 16, and 20). The average particle residence time is equal to the ionization time in the steady-state plasma, and this can be obtained from the spectroscopically determined electron temperature and the background

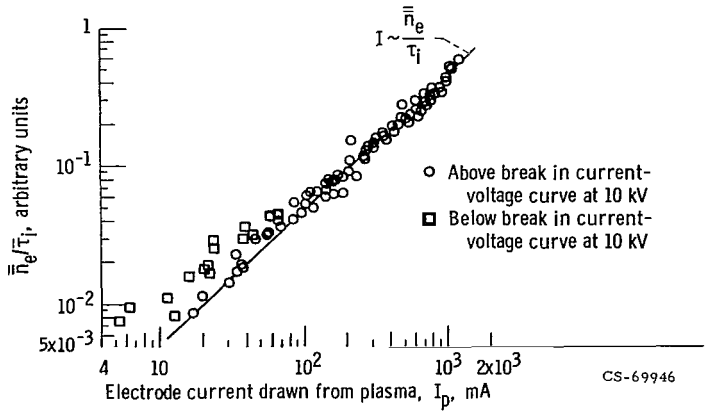

Figure 9. - Ratio of average electron number density to average particle containment time, determined spectroscopically, as function of electrode current flowing to plasma - low-pressure mode. Maximum magnetic field strength, B_{max}, 2.4 teslas; background helium density, n_0, $2.6x10^{11}$ to $24x10^{11}$ particles/cm^3 (8 to 89 μtorr).

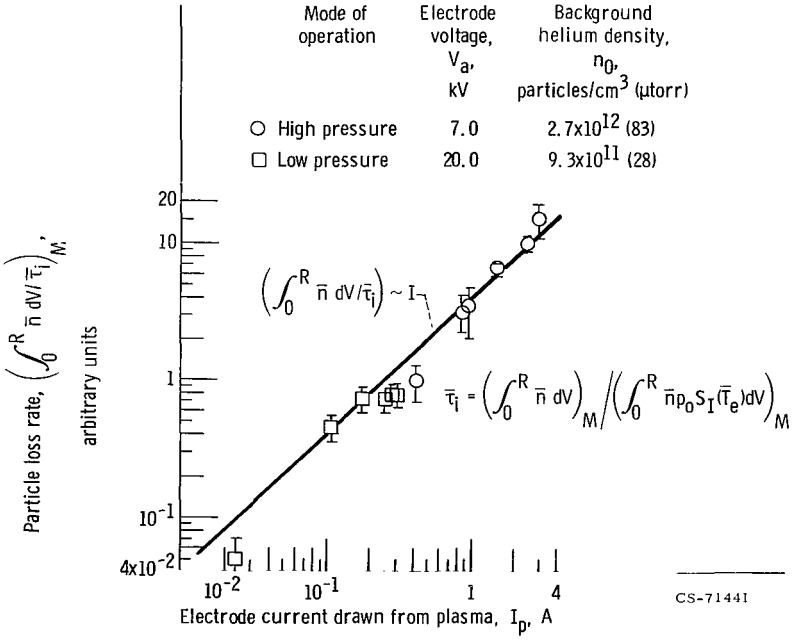

Figure 10. - Profile-integrated loss rate, determined spectroscopically, as function of current drawn from plasma for various numbers of electrode rings. Maximum magnetic field strength, B_{max}, 2.4 teslas.

neutral gas pressure. Figure 9 shows the ratio of the relative electron number density to the average particle residence time as a function of the total electrode current. The low-pressure-mode data exhibit a proportionality between the discharge current and the ratio of electron number density and residence time. Thus, the proportionality implied by equation (2) seems to hold to a reasonable approximation over two orders of magnitude in discharge current.

In figure 10 are some data taken from reference 16. In these data, radial profiles of electron temperature and number density were measured. The average relative number density is based on an average over these profiles. The ratio of the average relative number density to the particle residence time is directly proportional to the discharge current over at least two orders of magnitude in the discharge current. The data shown in figure 10 include both modes of operation and also different numbers of electrode rings, in which 12, 6, 3, and 1 electrode ring were used to generate the plasma (ref. 16).

The spectroscopic data shown in figures 9 and 10 support equation (2) to the extent that the discharge current is seen to be directly proportional to the ratio of the relative number density to the particle residence time. Unfortunately, it was not possible to determine the absolute number densities from the spectroscopic data, and we cannot rule out the (probably remote) possibility that the parasitic currents and/or ambipolar flows are a fixed fraction of the total electrode current over the entire range of electrode currents.

Supportive Scaling-Law Data

If the particle balance in the bumpy-torus plasma is determined by ionization of the background gas and loss through nonambipolar electrode currents, the equation of continuity for the electrons may be written as follows:

$$\frac{dn_e}{dt} = - \frac{I_p}{eV_p} + n_e n_0 \langle \sigma v \rangle_{ne} \tag{5}$$

In this steady-state plasma, the left side of equation (5) may be set equal to zero, implying that the plasma current will be equal to

$$I_p = eV_p n_e n_0 \langle \sigma v \rangle_{ne} \tag{6}$$

Thus, if the assumptions embodied in equation (5) are true, the plasma current will be proportional to the product of the electron and neutral number densities, as indicated in equation (6). If we plot the electrode current as a function of the density product, any systematic departure from a straight line would imply that the assumptions break down; that is, that the particles produced by ionization are carried away by ambipolar currents or by parasitic currents unrelated to ionization processes in the plasma.

A correlation study was reported in reference 12, in which the plasma current was correlated as a function of several variables. The plasma current was found to be a function of the electron and neutral particle number densities and the maximum magnetic field strength, as indicated in equation (7), taken from reference 12.

$$I_p = C_i n_e^{1.0} n_0^{1.10} B_{max}^{0.25} \tag{7}$$

Figure 11 shows some of these scaling-law data, in which the scaled current from

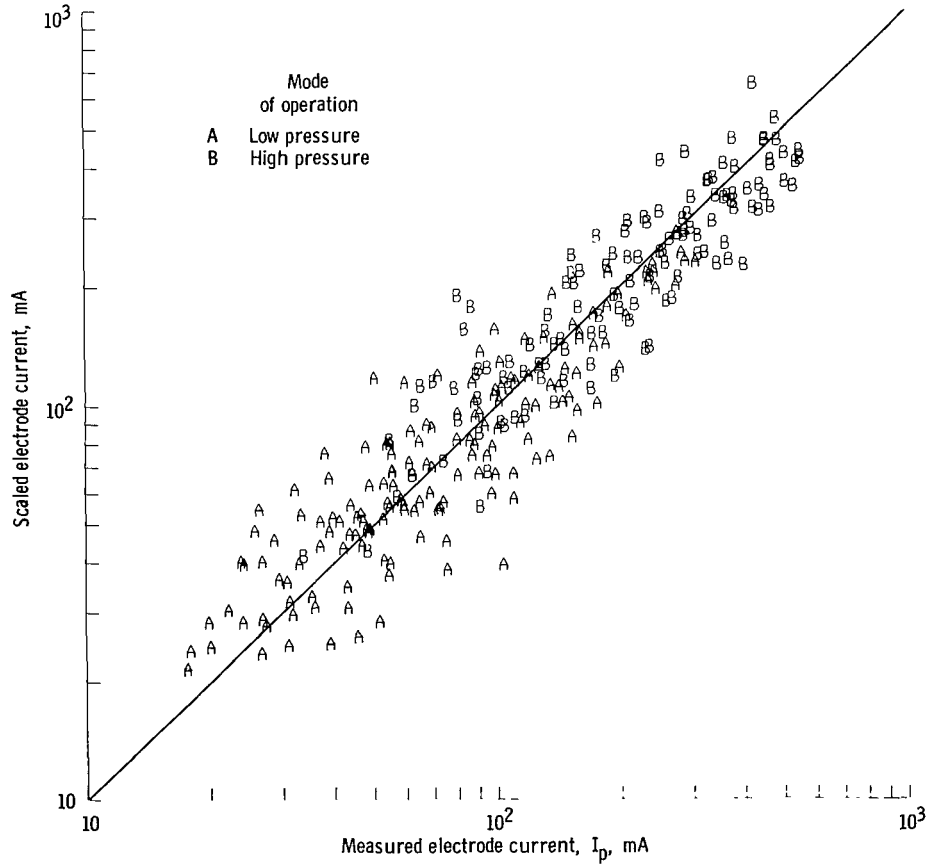

Figure 11. - Scaled electrode current from equation (7) as function of actually measured electrode current. (The relative electron number density appearing in the scaling law was determined by spectroscopic techniques for laboratory run series SN-TJ.)

equation (7) is plotted on the y-axis and the measured electrode current is plotted on the x-axis. The electron number densities were relative values determined spectroscopically. This scaling law is generally consistent with equation (6) and with the assumptions that there are no substantial parasitic currents that vary with operating conditions, that there are no ambipolar particle flows to the electrodes, and that the plasma is produced by volume ionization within the containment volume. Figure 12 shows correlation data that also are fit by equation (7) but in which the electron number density was measured by a radiofrequency emission technique described in reference 11. The correlated data are spread somewhat more widely in figure 12, but it does appear that equation (6) and the assumptions on which it is based are supported by the correlation data.

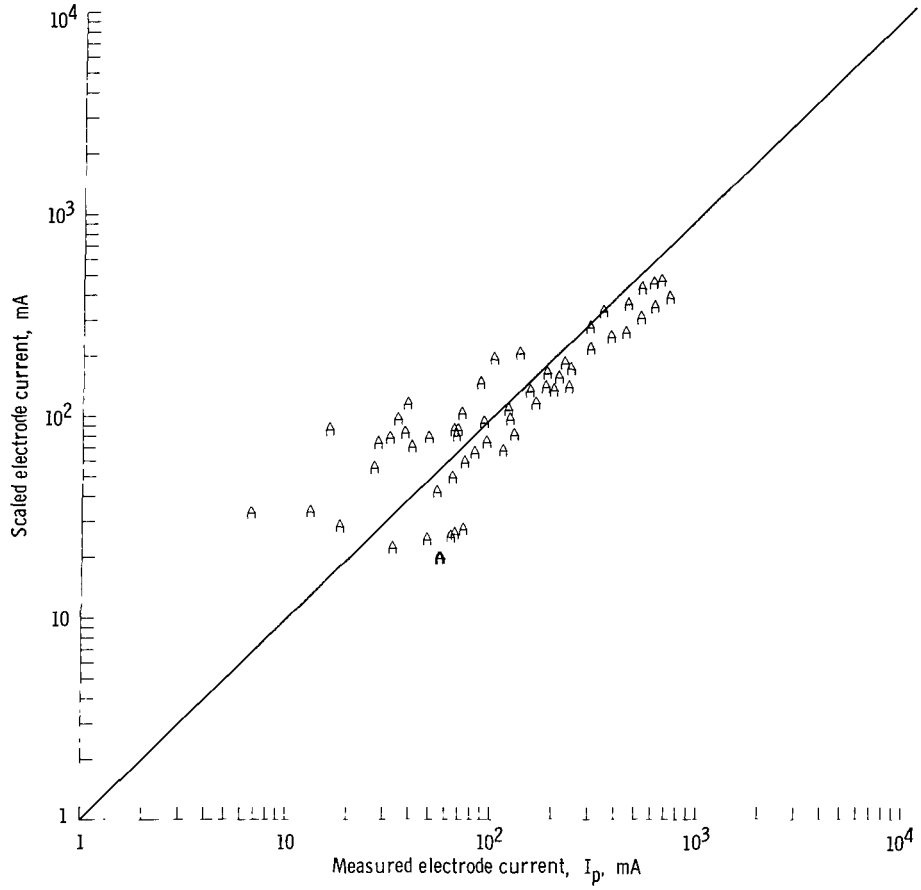

Figure 12. - Scaled electrode current from equation (7) as function of actually measured electrode current - low-pressure mode. (The absolute electron number density in the scaling law was determined by radiofrequency emission techniques.)

Direct Measurement of Parasitic Power Flux

The spectroscopic and correlation data in figures 9 to 12 are consistent with the assumption that the plasma is produced by volume ionization and that any parasitic or ambipolar currents which exist do not vary as a proportion of the total current over the range of operating conditions investigated. On the basis of these data, however, it is not possible to rule out the existence of a parasitic or ambipolar current that is a fixed fraction of the total current flowing to the power supply, independent of the operating conditions.

Accordingly, an experiment was performed that makes it possible to place an upper bound on the parasitic currents (but not the ambipolar currents) outside the plasma volume. This procedure was based on the fact that, in this steady-state experiment, uncooled sheet metal will melt above a critical incident power flux. The liquid-nitrogen-cooled coil shields were covered in two sectors by aluminum foil in the regions closest to the plasma. One set of these aluminum foil sheets is shown in figure 13. Uncooled sheet metal that is bombarded by parasitic currents will heat up until it reaches an equilibrium temperature determined by its emissivity and the Stefan-Boltzmann radiation law

$$W_{pa} = \epsilon \sigma T_m^4 \qquad W/m^2 \tag{8}$$

If the incident parasitic power flux W_{pa} is increased, the temperature will rise to the melting point T_m of the sheet metal. For aluminum, the AIP handbook (ref. 21) lists a T_m of 933 K and an emissivity ϵ of 0.04 for molten aluminum at 1000 K. The CRC handbook (ref. 22) lists an emissivity for aluminum of 0.06 at 500 K and an emissivity for oxidized aluminum foil of 0.19 at 500 K. Taking the conservative value of 0.19 and substituting the melting temperature into equation (8) yields a critical power flux of 0.82 W/cm^2 to melt uncooled aluminum foil.

The power dissipated in the plasma was increased to progressively higher levels until the aluminum foil was seen to glow red hot and begin to melt. When the aluminum foil began to melt, the power supply was delivering 42.7 kilowatts to the plasma. The melting damage shown in figure 13 and in more detail in figure 14 occurred when the power input was further raised to 60 kilowatts. The area of melted aluminum foil in figures 13 and 14 was measured with a planimeter and found to be 7.8 square centimeters. There are 12 sectors in the torus, and so the total area subjected to the critical power flux is given by equation (9):

$$P_W = 12 W_{pa} A \tag{9}$$

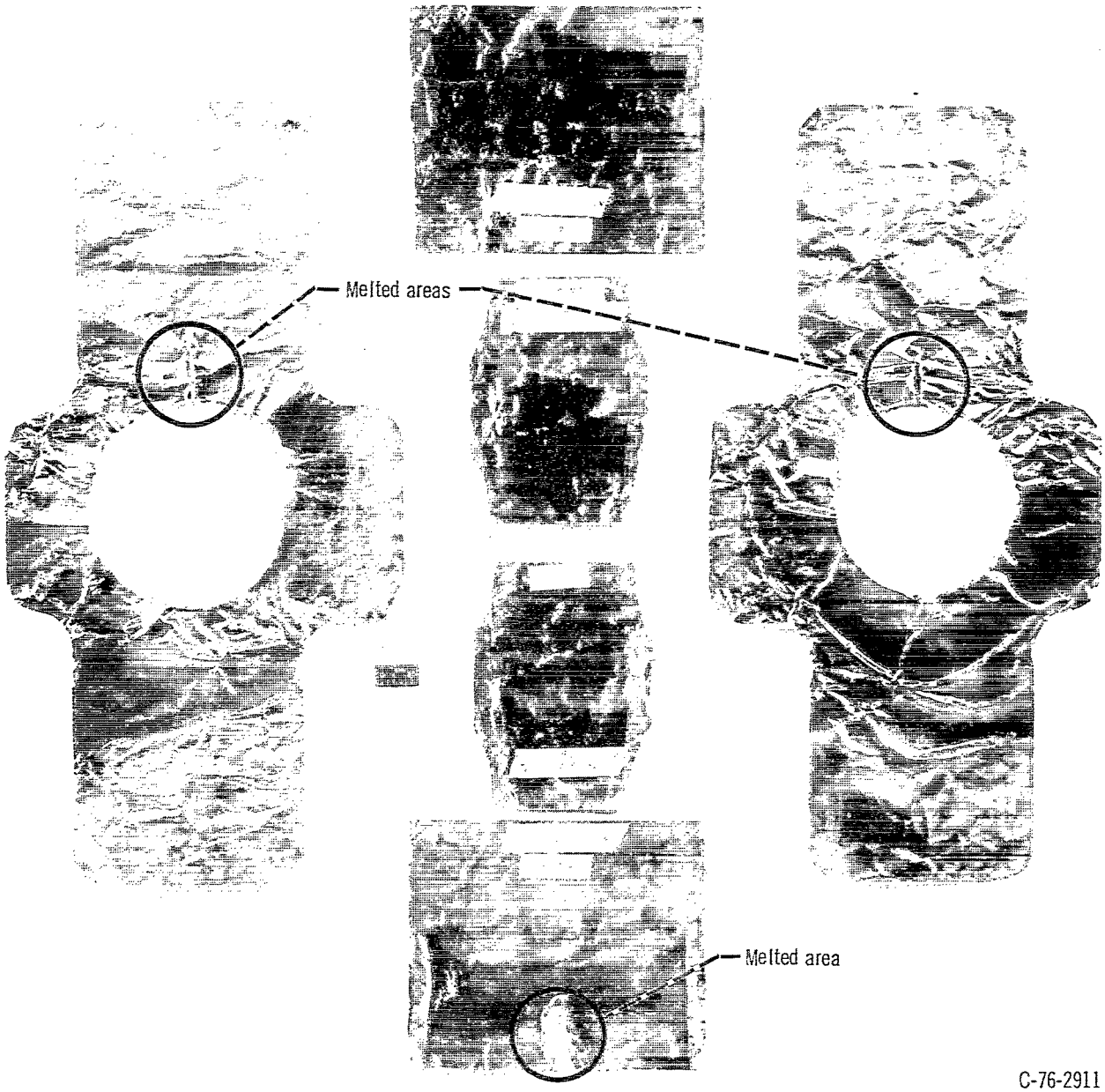

Figure 13. - Aluminum foil that surrounded plasma in sector 10. (Note the three small areas in which the aluminum foil melted when 60 kW were dissipated by the plasma.)

If we take this melted area as being characteristic of the area bombarded by the critical flux, which occurred at 42.7 kilowatts, it becomes possible to estimate the total current flowing to the sheet metal. There are 12 sectors in the bumpy torus, each of which presumably experience 7.8 square centimeters of melting at a critical power flux of 0.82 W/cm^2. This adds up to a total power of 77 watts to the sheet metal surrounding the plasma volume as a result of parasitic currents not flowing to the plasma itself.

The melted areas shown in figures 14(a) and (b) occurred on the side planes of the coils and represent the projection of the anode ring support rod on the sheet metal (which is shown in fig. 1). Figure 14(c) shows the cover of the lower outer spacer bar. The other three spacer bar covers shown in figure 13 were not melted.

These aluminum foil melting tests revealed that no more than 77 watts of parasitic current were flowing to the surrounding sheet metal at a time when the total plasma power was 42.7 kilowatts. This power represented an anode voltage of 10 kilovolts and an anode current of 4.27 amperes. Since the aluminum foil sheet is, in effect, a cathode surface at ground potential, it will be struck by ions generated somewhere between the electrode ring support rod at potential $+V_a$ and the grounded surface. It is probable, because of the strong electric field concentrations near the anode ring, that the ionization occurs near the anode ring and hence that the ions have very nearly the anode potential. We will assume, however, that the ions are created more or less uniformly along the magnetic field lines that connect the anode ring structure to the grounded aluminum foil. The appropriate energy of ions bombarding the aluminum foil is therefore one-half of the electrode voltage.

The relation between the total parasitic power of 77 watts from equation (9) and the assumed parasitic energy and current is

$$P_W = 77 \text{ watts} \approx \frac{1}{2} V_a I_{pa} \tag{10}$$

where the anode voltage was 10 kilovolts in this case. Solving for the parasitic current yields a total current of 15 milliamperes, when the total current flowing to the plasma was 4.27 amperes. That is, only 4/10 of 1 percent of the net current flowing from the power supply was devoted to currents flowing outside the plasma volume. This estimate is probably an upper bound, because the emissivity of aluminum is likely to be less than the value of 0.19 assumed for oxidized aluminum; because the melting shown in figures 13 and 14 occurred at 60 kilowatts of input power rather than the 42.7 kilowatts at which the melting just started to occur and which was used in these computations; and because the ions probably had energies greater than one-half of the anode potential as they moved from the anode ring structure to the cathode.

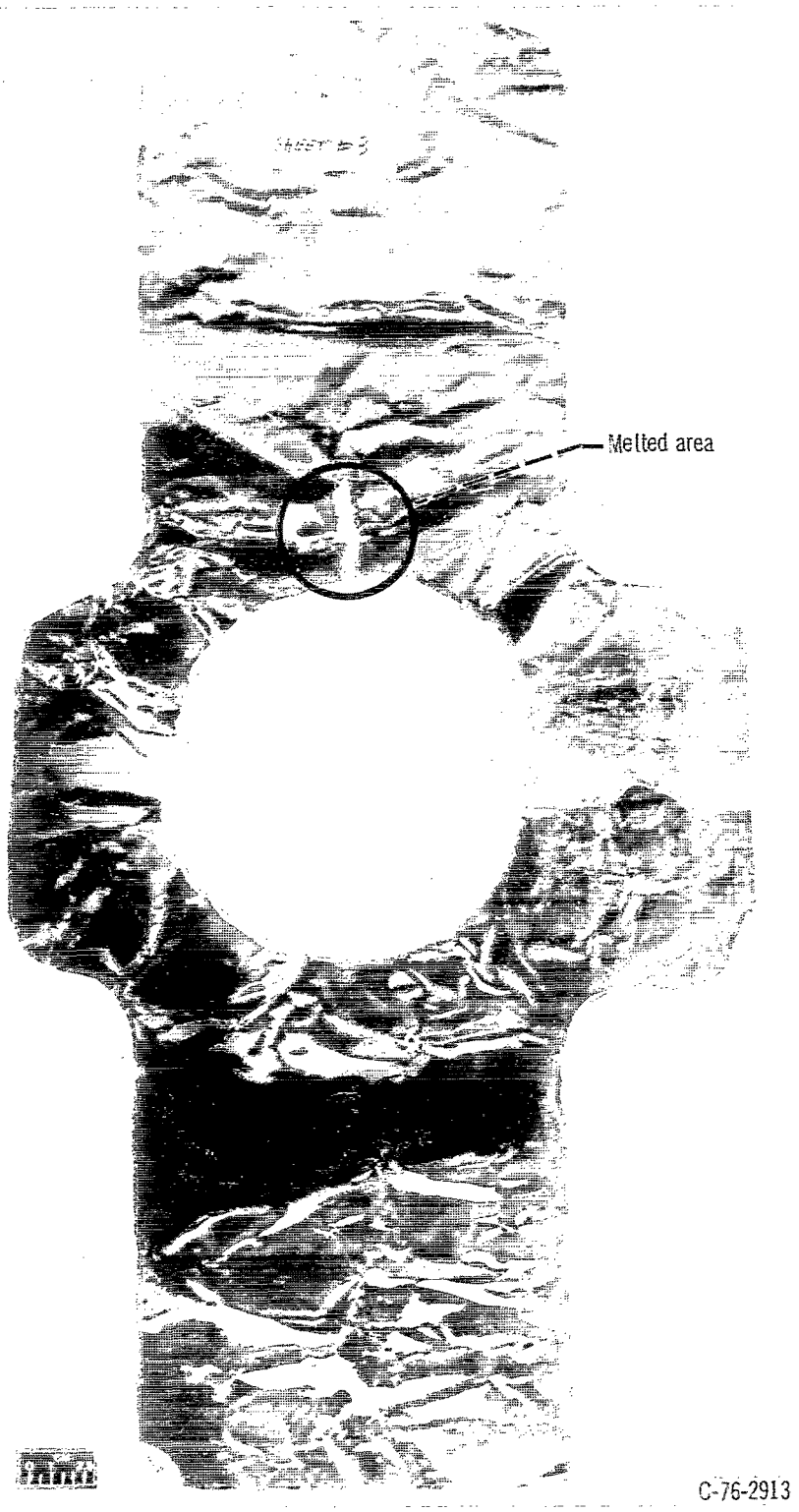

(a) Aluminum foil on coil 10.

Figure 14. - Closeup views of melted aluminum foil shown in figure 13.

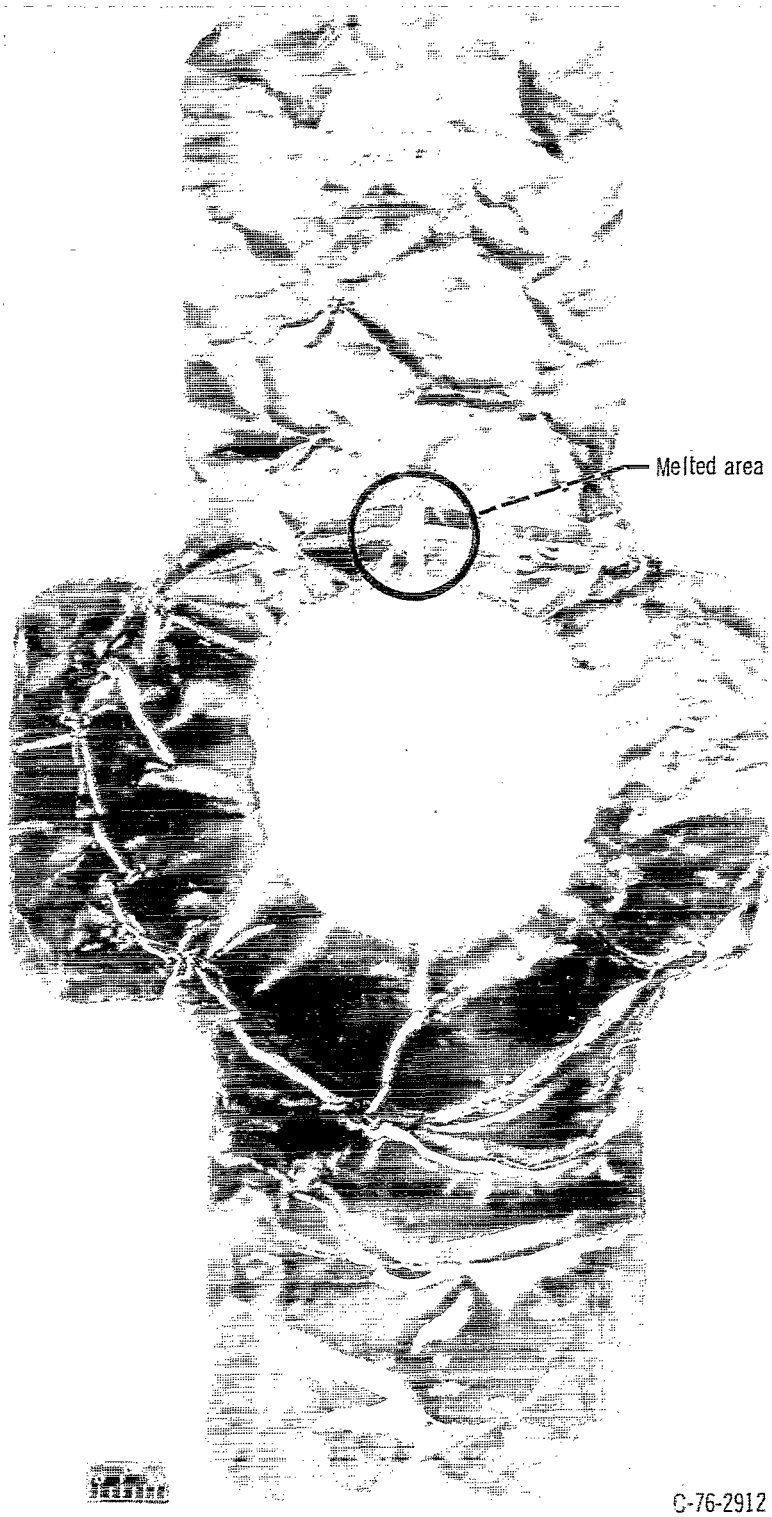

(b) Aluminum foil on coil 11.

Figure 14. - Continued.

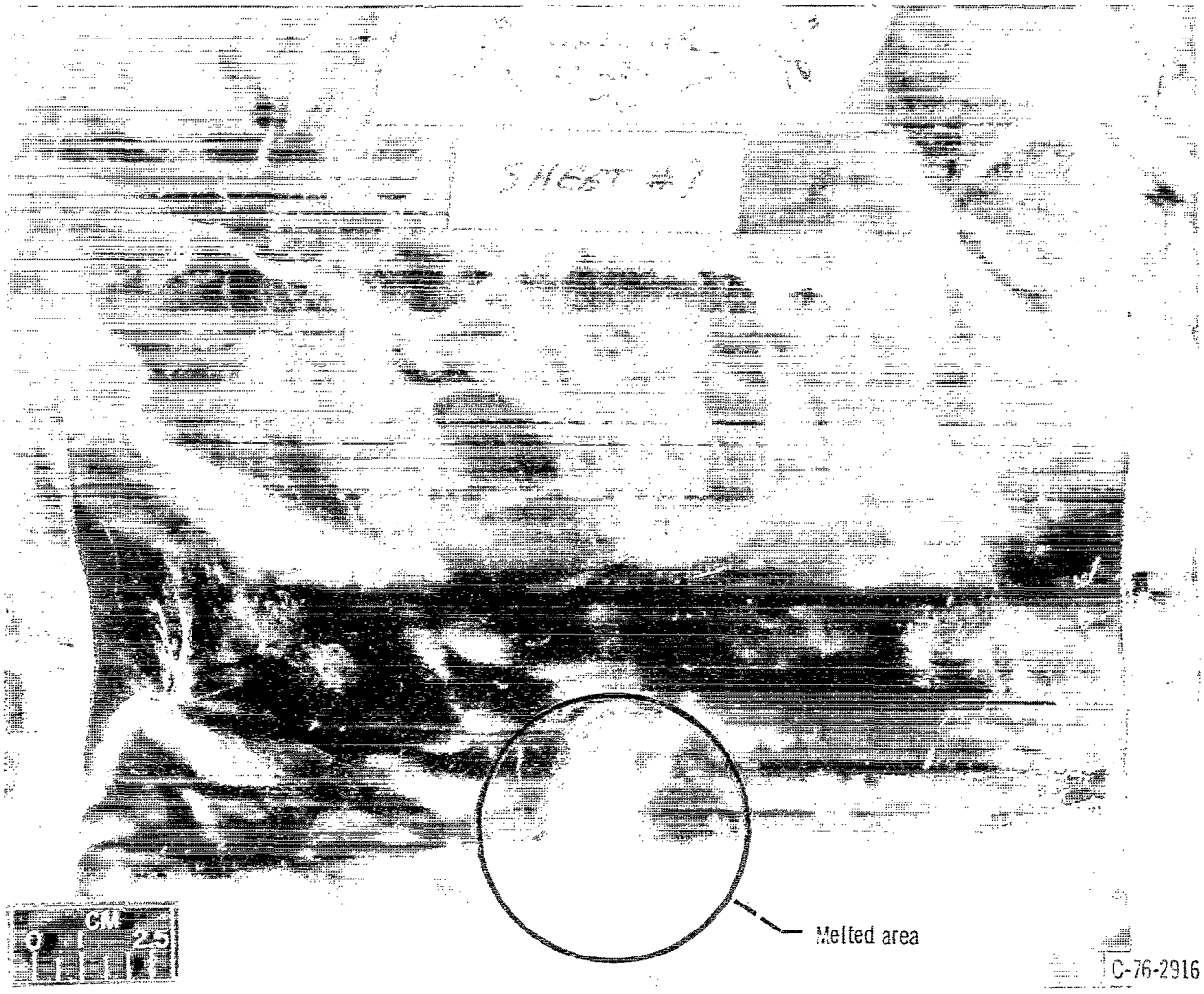

(c) Aluminum foil on lower outer spacer bar.

Figure 14. - Concluded.

A similar experiment was performed with a negative potential on the midplane electrode rings. With the electric fields reversed, the parasitic power fluxes were even less than with positive midplane electrode rings. No melting or heating to a red-hot condition was observed with the midplane electrode rings negative, up to a power input of 40 kilowatts.

These data lend support to the assumption that no significant parasitic currents flow outside the plasma volume. There is no significant melting, heating, or other damage to the sheet metal and other structures in the vicinity of the electrode ring support rods, and the small amount of damage documented in figures 13 and 14 is consistent with a parasitic current substantially less than 1 percent of the total current flowing to the

power supply. For purposes of calculating the particle and energy containment times using equations (2) and (4), these parasitic currents will be neglected as a small second-order effect.

TOROIDAL SYMMETRY OF PLASMA

Both the microwave interferometer and the charge-exchange neutral detector are relatively immobile and are not moved from one sector to another of the plasma. For this reason, it is essential to be sure that the sectors in which they are located are characteristic of the toroidal plasma as a whole. Effects of varying the number of electrode rings must be separated from effects of the presence or absence of an electrode ring in the sector in which the diagnostic instrument is located or from the number of empty sectors between the instrument and the nearest electrode ring. Before a definitive determination of the scaling laws of this plasma could be made and before the plasma operating parameters could be optimized, the existence of toroidal symmetry had to be assured. Otherwise, the effects due to the nonsymmetry of the plasma had to be known, in order to be taken into account in later measurements.

Toroidal Symmetry of Electrode Current

The current flowing to each of the 12 midplane electrode rings in the normal 12-electrode configuration was measured by individual current meters on each electrode ring. It was found that small variations in the alinement and vacuum leaks in a particular sector did produce substantial asymmetries in the current drawn by the 12 midplane electrode rings. Figure 15 shows the current drawn by each of the 12 midplane electrode rings with positive polarity, for several values of the electrode voltage and the high- and low-pressure modes of operation. The residual asymmetry in the current drawn is about a factor of 2 in this case. In figure 16 are shown the currents drawn by the the 12 midplane electrode rings under the same conditions as those in figure 15, but with negative polarities. The current drawn by the negative electrode rings was much more symmetric than that drawn by the positive electrode rings. The characteristic results in figures 15 and 16 were also found to hold at other background neutral gas pressures, for helium as well as deuterium gas, and for fewer than 12 electrode rings. Data were taken for six and three electrode rings. The current was found to be divided equally among the electrode rings, with the exception of three negative electrode rings, for which a plasma could not be generated.

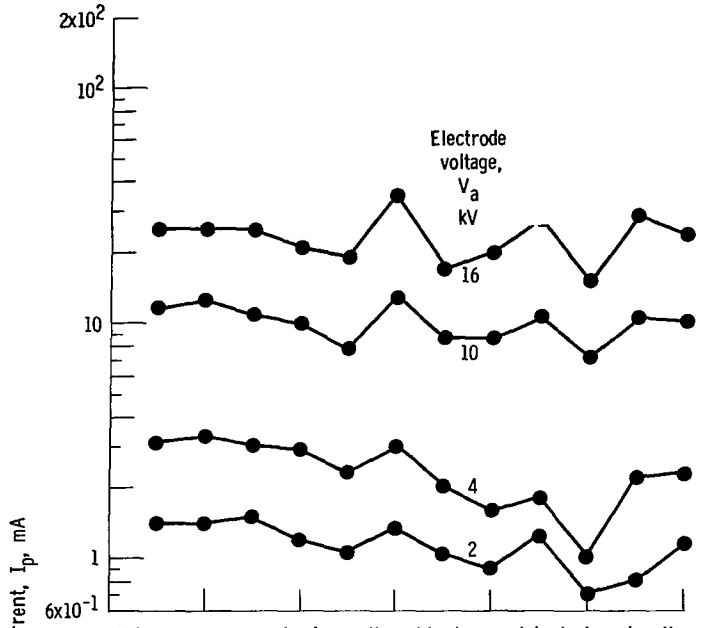

(a) Low-pressure mode of operation at background deuterium density n_0 of 6.6×10^{11} particles/cm^3 (20 μtorr).

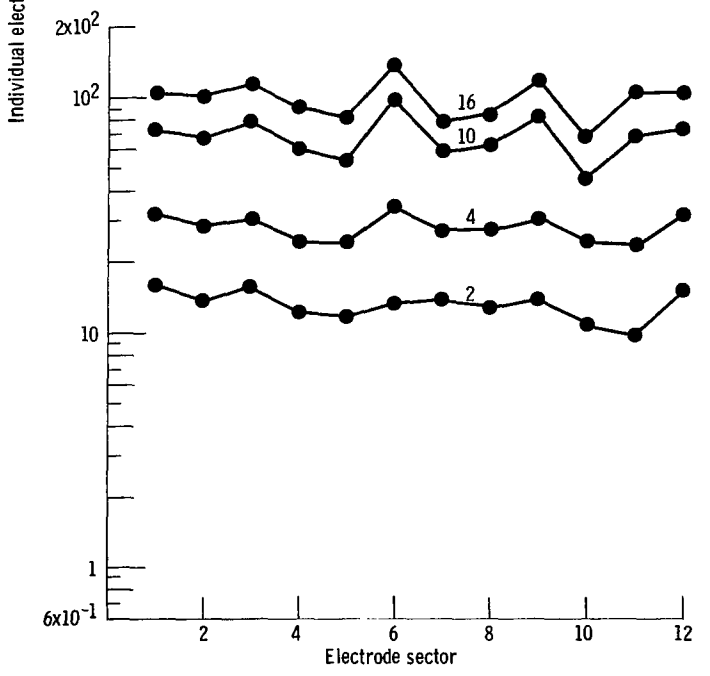

(b) High-pressure mode of operation at background deuterium density n_0 of 1.7×10^{12} particles/cm^3 (51 μtorr).

Figure 15. - Uniformity with which current is collected by the 12 individual electrode rings with positive electrode polarities. Maximum magnetic field strength, B_{max}, 2.4 teslas.

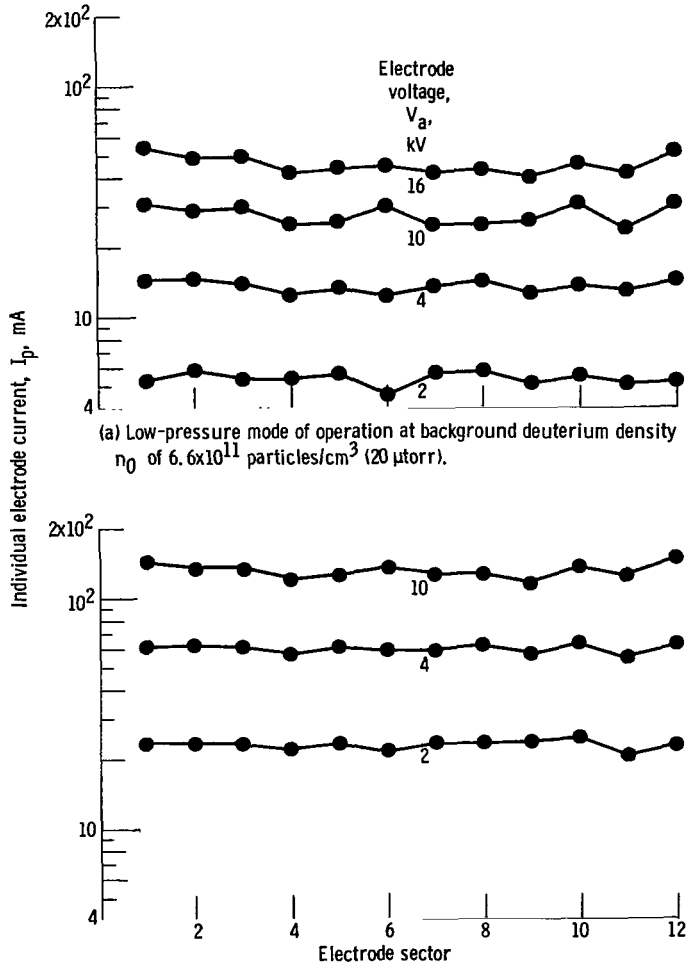

(a) Low-pressure mode of operation at background deuterium density n_0 of 6.6×10^{11} particles/cm^3 (20 μtorr).

(b) High-pressure mode of operation at background deuterium density n_0 of 1.7×10^{12} particles/cm^3 (50 μtorr).

Figure 16. - Uniformity with which current is collected by the 12 individual electrode rings with negative electrode polarities. Maximum magnetic field strength, B_{max}, 2.4 teslas.

Toroidal Symmetry of Plasma Number Density

Figure 17 shows the numbering convention of the sectors of the NASA Lewis bumpy torus and the location of the microwave interferometer and the neutral particle energy analyzer. When ion kinetic temperature or number density measurements were taken, a baffle plate was inserted on the major axis of the torus to prevent any influence from the plasma at the opposite end of a toroidal diameter.

The microwave interferometer is located in sector 10. The effect on measured number density in sector 10 of moving a single positive midplane electrode ring from

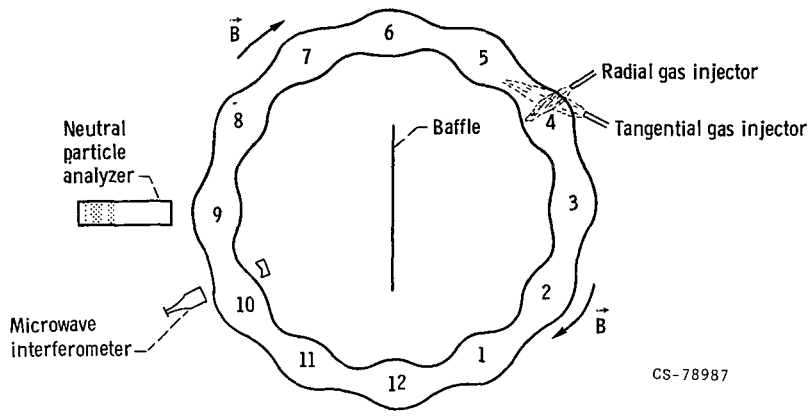

Figure 17. - Sketch showing numbering convention of the 12 sectors of the NASA Lewis bumpy torus. (The microwave interferometer is located in sector 10, the charge-exchange neutral detector in sector 9, and the neutral gas jets in sector 4.)

that sector around the torus was investigated. Figure 18 shows the electron number density measured for constant operating conditions in both modes of operation as the midplane electrode ring was moved successively around the torus. The variations in

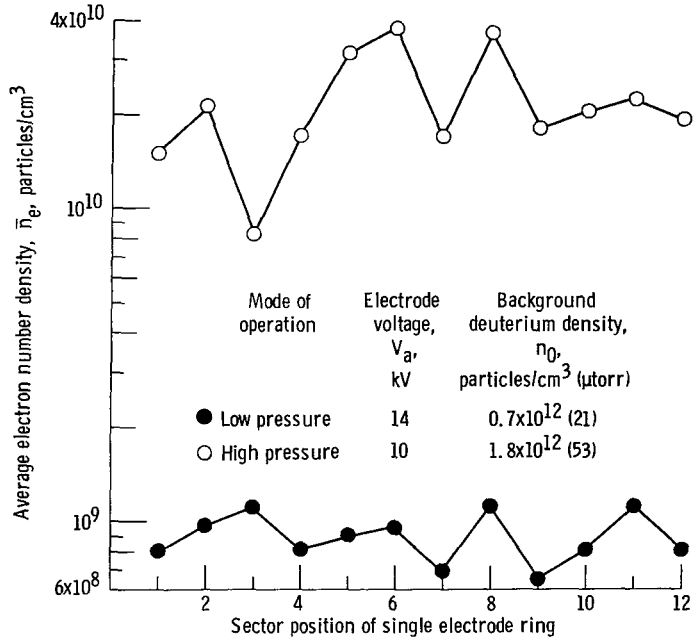

Figure 18. - Average electron number density as function of sector position of a single anode ring. (The number on the x-axis designates the sector in which the electrode was located.) Positive polarity; maximum magnetic field strength, B_{max}, 2.4 teslas; deuterium gas.

electron number density shown in figure 18 are larger for the high-pressure mode than for the low-pressure mode, but neither exhibits any tendency of the density to fall off as the anode ring becomes more remote from the microwave interferometer.

Factors that Perturb Toroidal Symmetry

Two principal factors, in addition to the presence or absence of electrode rings, perturb the toroidal symmetry of the plasma. These two factors include (1) the presence of a gas leak in the vicinity of the sector in question and/or the method of neutral gas injection and (2) misalinement of the midplane electrode ring relative to the magnetic field lines and other electrode rings.

The effect of misalining an electrode ring is illustrated by the current-voltage curves in figure 19. The data in this figure are for helium gas at a background density of 9.3×10^{11} particles/cm^3 (28 μtorr) with one electrode ring operated with positive polarity in sector 1. This single electrode ring was displaced about its nominal position, and the effects on the current-voltage curve were studied. The nominal position is shown by the diamond-shaped symbols. The midplane electrode ring was translated 2.5 centimeters along the axis of the plasma parallel to the midplane, and the current-voltage curve shown by the square symbols resulted. In some cases, the current rose by a factor of 2 or more above the nominal value from the effects of this displacement. The electrode ring was then moved back to the midplane and retracted, with its center 2 centimeters above the equatorial plane of the torus. The curve shown by the triangular symbols resulted. In this case, the current increased by as much as a factor of 3 above the nominal currents obtained in the equatorial and midplane positions. The electrode ring was pushed 2 centimeters below the equatorial plane of the torus, and the current-voltage curve shown by the circular symbols resulted. In this case, the currents averaged as much as 30 percent lower than the nominal value. It was found that motion of the midplane electrode ring radially inward and outward in the midplane did not substantially affect the current-voltage curves and that rotating the electrode ring by as much as 15 degrees about its vertical axis also did not substantially affect the current-voltage curves. Although the current-voltage curves were not affected by displacements along the major toroidal radius, there is reason to expect both plasma number density and containment time to be affected, as discussed later.

The presence of a neutral gas concentration in one of the sectors substantially perturbs the plasma in that sector. Figure 20(a) shows some data for deuterium gas similar to that shown in figure 16(b), in which 12 negative electrode rings were used. In figure 20(a) the neutral deuterium gas flowing into the vacuum tank was injected on the major axis of the vacuum tank in a symmetric manner. In this case, the variation of the current drawn is relatively small from sector to sector. Figure 20(b) shows the

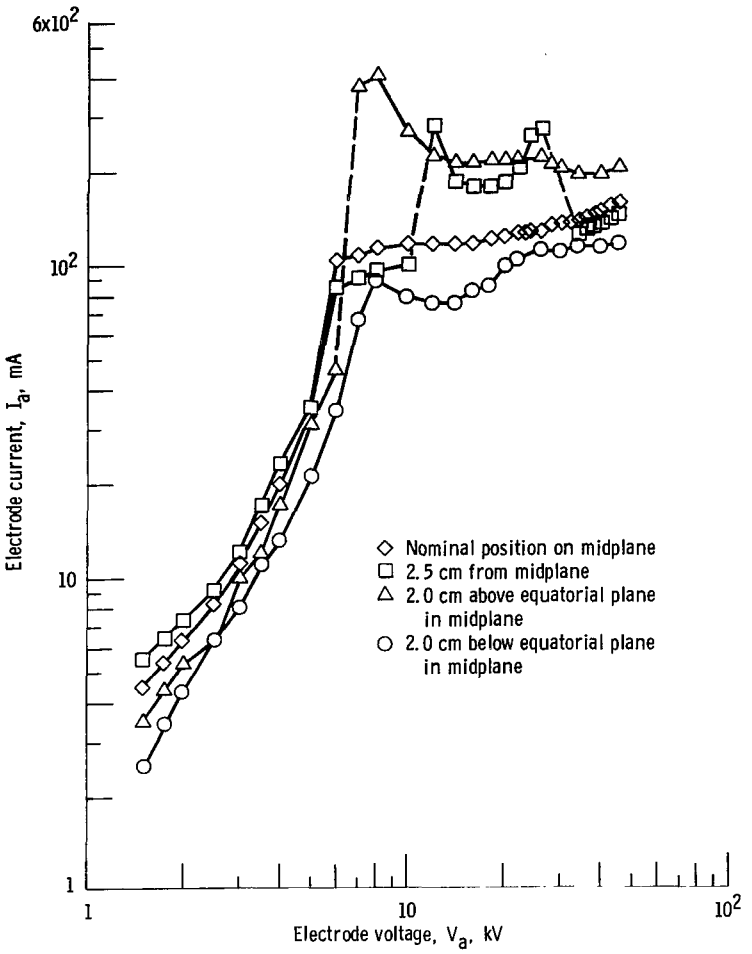

Figure 19. - Current-voltage curves for maximum magnetic field strength B_{max} of 2.4 teslas, positive electrode polarity, and a background helium density n_0 of 9.3×10^{11} particles/cm^3 (28 μtorr). (The four curves represent the nominal position and three deliberate misalinements of an electrode ring from its nominal position.)

current drawn by the individual electrode rings under the same plasma operating conditions but with neutral gas injected across the minor plasma diameter in sector 4. Relative to the axial gas injection in figure 20(a), there is a substantial increase in electrode current, amounting to about 50 percent, in the sector in which the gas is injected. There is also a slight increase in the current drawn in the two adjacent sectors of the torus. Figure 20(c) shows the current drawn by individual electrode rings under the same plasma operating conditions as the two preceding figures but with the neutral deuterium gas injected tangential to the plasma torus in sector 4. In this case, the current drawn is increased by nearly a factor of 2 in sector 4, in which the gas is injected, and the downstream sectors 5 and 6 also have their currents enhanced substantially by the localized jet of neutral gas.

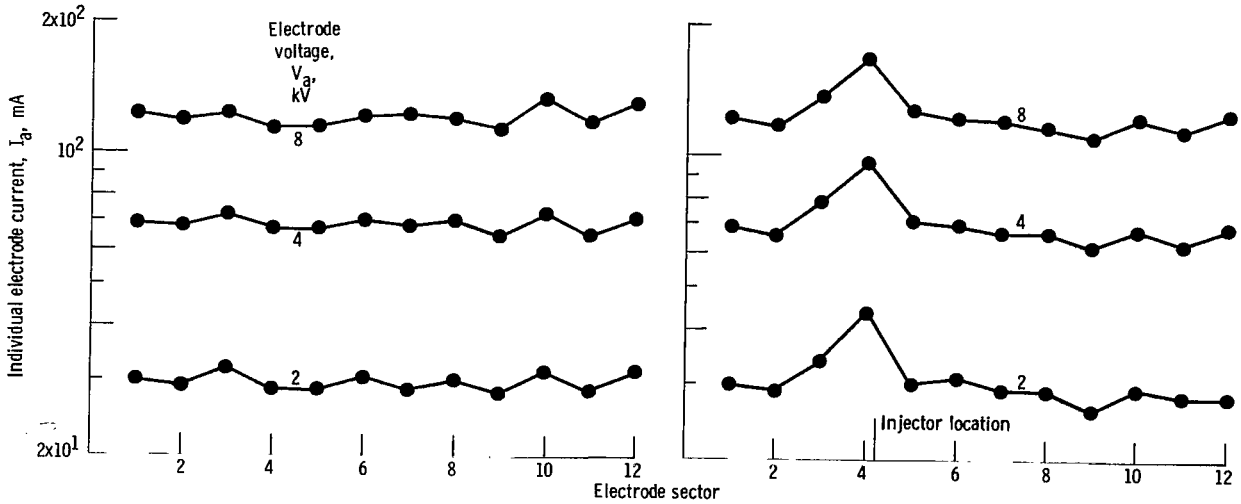

(a) Symmetric axial injection of deuterium into vacuum tank.

(b) Deuterium gas injected along a minor radius of the plasma in sector 4.

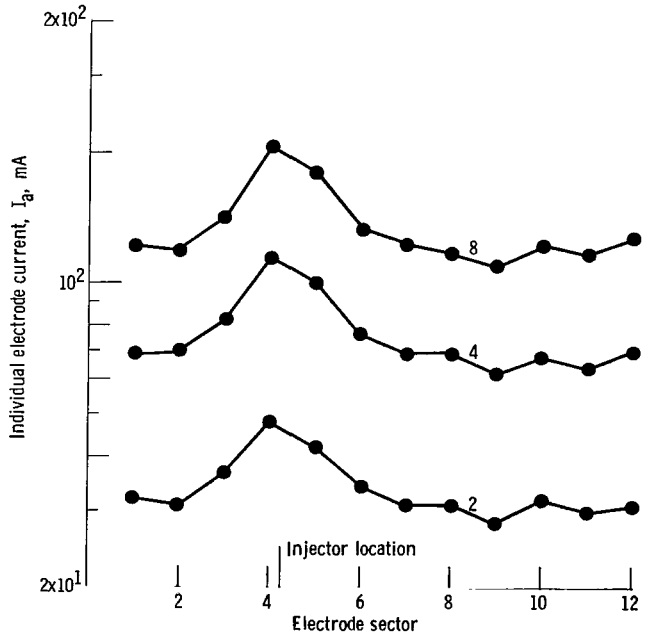

(c) Deuterium gas injected tangentially to the plasma torus at sector 4.

Figure 20. - Uniformity with which current is collected by the 12 individual electrode rings for three modes of deuterium injection into vacuum tank. Negative polarity; background deuterium density, n_0, $1.3x10^{12}$ particles/cm^3 (40 μtorr); maximum magnetic field strength, B_{max}, 2.4 teslas.

Unless otherwise stated, the data in this report were taken under conditions in which the neutral gas was injected on the tank axis in the manner represented by figure 20(a). The presence of a leak in the water or cryogenic systems in one sector of the torus was capable of creating a perturbation in the toroidal symmetry of the plasma. Care was taken to eliminate even small gas leaks in the vicinity of the plasma when publishable data were taken from this experiment.

EFFECTS OF ELECTRODE RING CONFIGURATION

Geometries Investigated

Obtaining valid scaling laws and parametric optimization studies requires accounting not only for possible effects of toroidal asymmetry, but also for any effects that depend on how well the plasma communicates around the torus. If the standard plasma configuration with 12 electrode rings is symmetric around the torus, as was shown in the previous section, we must also know whether the number of electrode rings or the distance between the electrode rings and the diagnostic instruments affects the density and temperature. If the density or temperature depended on the distance of the nearest electrode ring from the appropriate diagnostic instrument, this factor would have to be allowed for in any optimization study in which either the configuration or the number of electrode rings was varied.

To investigate this latter point, three different configurations of the electrode rings were used, as shown in table I. In configuration I, measurements of ion density and kinetic temperature were made with all 12 electrode rings in place. After this, the electrode ring immediately opposite the microwave interferometer in sector 4 was removed. Then the three electrodes most distant from the microwave interferometer were removed. This procedure was repeated until only the electrode ring in front of the microwave interferometer in sector 10 remained. Configuration II is, in a sense, the mirror image of configuration I. Measurements were started with all 12 electrodes in place, then only the electrode ring in front of the microwave interferometer in sector 10 was removed, and then the electrode rings were removed in pairs, until finally only the electrode ring opposite the major diameter from the microwave interferometer remained in sector 4. Configuration III consisted of symmetric arrangements of the electrode rings, in which data were first taken with all 12 electrode rings, then the electrode ring in front of the charge-exchange neutral detector in sector 9 was removed, then two symmetric groups of five electrode rings remained, and then three groups of three electrode rings. Penultimately, there were only two electrode rings in sectors 4 and 10 at opposite ends of the diameter, and finally only the electrode ring in sector 10 remained.

TABLE I. - THREE DISTINCT CONFIGURATIONS OF ELECTRODE RINGS USED WHEN THE NUMBER OF ELECTRODE RINGS WAS VARIED

Number of electrodes	Sector											
	1	2	3	4	5	6	7	8	9	10	11	12
Configuration I												
12	×	×	×	×	×	×	×	×	×	×	×	×
11	×	×	×		×	×	×	×	×	×	×	×
9	×	×				×	×	×	×	×	×	×
7	×						×	×	×	×	×	×
5								×	×	×	×	×
3									×	×	×	
1										×		
Configuration II												
12	×	×	×	×	×	×	×	×	×	×	×	×
11	×	×	×	×	×	×	×	×	×		×	×
9	×	×	×	×	×	×	×	×				×
7	×	×	×	×	×	×	×					
5		×	×	×	×	×						
3			×	×	×							
1				×								
Configuration III												
12	×	×	×	×	×	×	×	×	×	×	×	×
11	×	×	×	×	×	×	×	×		×	×	×
10	×	×		×	×	×	×	×		×	×	×
9		×	×	×		×	×	×		×	×	×
8	×	×		×	×		×	×		×	×	
6		×		×		×		×		×		×
4	×			×			×			×		
3		×				×				×		
2				×						×		
1										×		

These three configurations were designed to exhibit any effects on the placement of the electrode rings with respect to the diagnostic instruments. Data were taken in both the high- and low-pressure modes of operation and for positive and negative polarities of the midplane electrode rings.

Effect of Configuration on Electron Number Density

The average electron number density measured in sector 10 is shown in figure 21(a) as a function of the number of positive electrode rings used and for the three configurations shown in table I. Variations of a factor of 2 in number density are probably not significant and result from subtle changes in operating conditions of the kind responsible for the time-dependent number density variations discussed later in connection with figure 23(b). In both modes of plasma operation, there appeared to be no significant differences between the configurations used; the plasma communicated quite well around the torus and the densities appeared to depend only on the number of anode rings and not on their configuration or placement with respect to the diagnostic instruments. In the low-pressure mode of operation, the electron number density did not seem to depend significantly on the number of midplane electrode rings used. In the high-pressure mode of operation, however, the electron number density appeared to increase by about a factor of 5 to 7 as the number of midplane electrode rings was decreased from 12 to 1. This is in good agreement with previous spectroscopic data (ref. 1, fig. 34) in both modes of operation, except for the high-pressure-mode data with one electrode ring. The discrepancy for this case is probably due to the inability to aline the electrode rings along the major radius of the torus in the previous work. A larger number of positive electrode rings is detrimental to plasma confinement. This suggests that the electrode rings with the existing radial alinement (illustrated, e.g., in fig. 6) are actually impairing plasma confinement.

Figure 21(b) shows the average electron number density as a function of the number of negative electrode rings used in the three configurations listed on table I. Data were taken for the same electrode voltages and neutral gas pressures used in figure 21(a). There are significant differences from the case of positive electrode polarities. First of all, if the negative electrodes are not in adjacent sectors, as is the case in configuration 3, a plasma cannot be generated with fewer than six electrode rings. In configurations 1 and 2, where the remaining electrodes are adjacent to each other, it is possible to generate a plasma with as few as two negative electrode rings in adjacent sectors. With negative polarities, there is not an order-of-magnitude difference in the plasma density in the low- and high-pressure modes of operation, as there is with positive polarities. In the low-pressure mode of operation, the electron number density decreases as the number of electrode rings decreases, but the situation is more complicated in the high-pressure mode. In the high-pressure mode, there appears to be a variation in the electron number density around the torus, since the curves for configurations I and II diverge. The significance of this is that in configuration II the last electrode rings in place were furthest from the microwave interferometer, and in configuration I the last electrode rings in place were closest to the microwave interferometer. This suggests that, with negative electrode polarities, some physical process

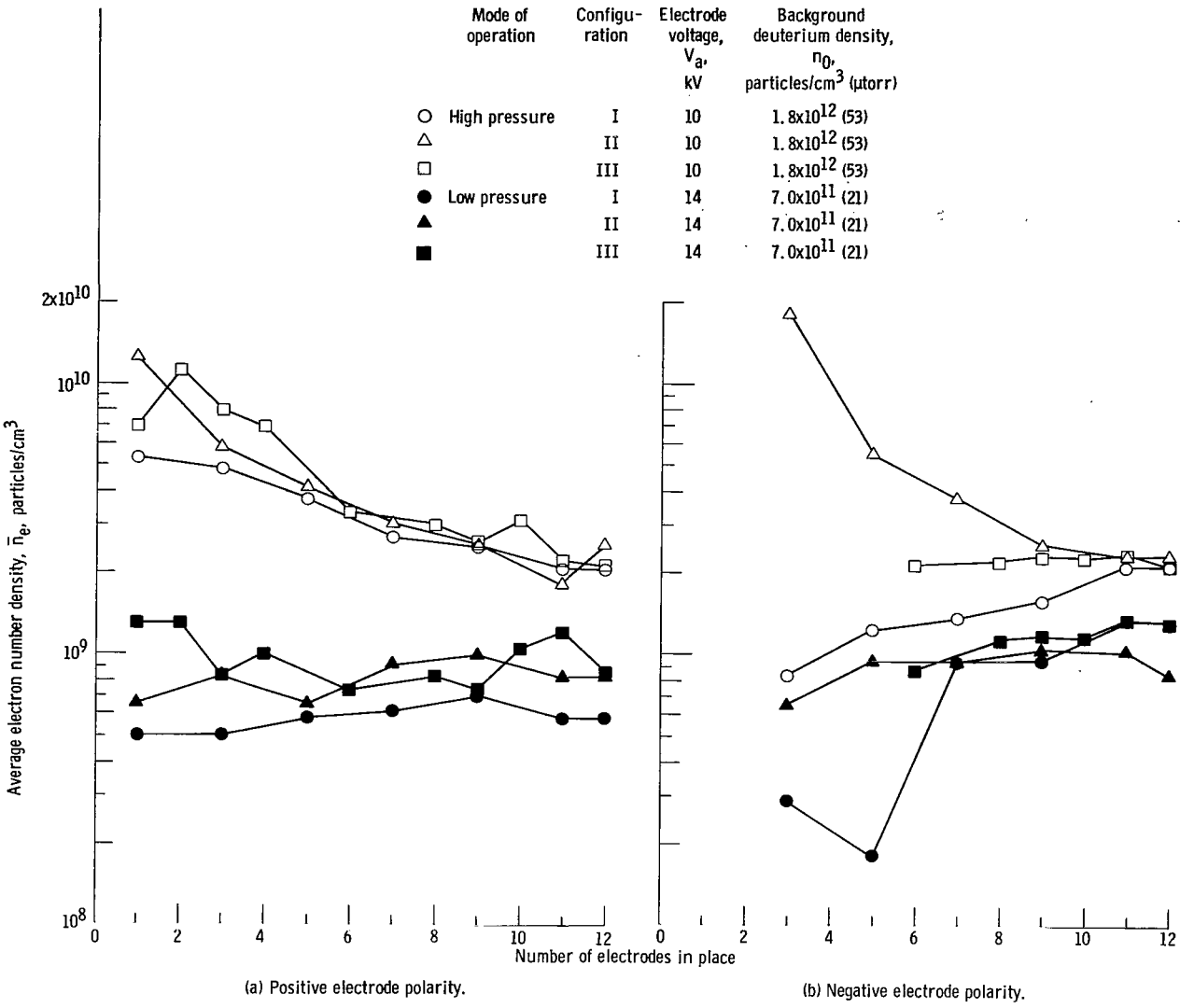

Figure 21. - Average electron number density as function of electrode ring configurations listed in table I for two background deuterium densities. Maximum magnetic field strength, B_{max}, 2.4 teslas.

associated with the presence of an electrode ring causes plasma loss and decreases the electron number density.

Effect of Configuration on Ion Kinetic Temperature

At the same time that the data in figure 21 were taken, the ion kinetic temperatures were measured with the charge-exchange neutral detector located in sector 9. The result of these measurements for positive polarities of the three electrode configurations listed in table I is shown in figure 22(a). The trends of the data are complex, but it appears that as the number of electrode rings is decreased in both the high- and low-pressure modes of operation, the ion kinetic temperatures drop off and then, in some cases, recover to their initial values as the number of electrodes is further reduced below about four. The only exception to this was the low-pressure mode of operation in configuration I, for which the ion kinetic temperature increased as the number of electrode rings was decreased.

Figure 22(b) shows ion kinetic temperature data taken under similar conditions but with negative electrode polarities. With fewer than seven electrodes in the system, either it was not possible to generate the plasma or the signal-to-noise ratio of the charge-exchange neutral detector was not high enough to permit data reduction. What data are available in figure 22(b) suggest that in the low-pressure mode of operation the ion kinetic temperature increases with a decreasing number of electrode rings and that, in the high-pressure mode of operation, the ion kinetic temperature decreases slightly as the number of midplane electrode rings is reduced. With both electrode polarities, there appears to be a significant effect on ion kinetic temperature of the number and configuration of electrode rings used to generate the plasma. The electrode ring configuration therefore must be considered in any optimization study of ion kinetic temperature.

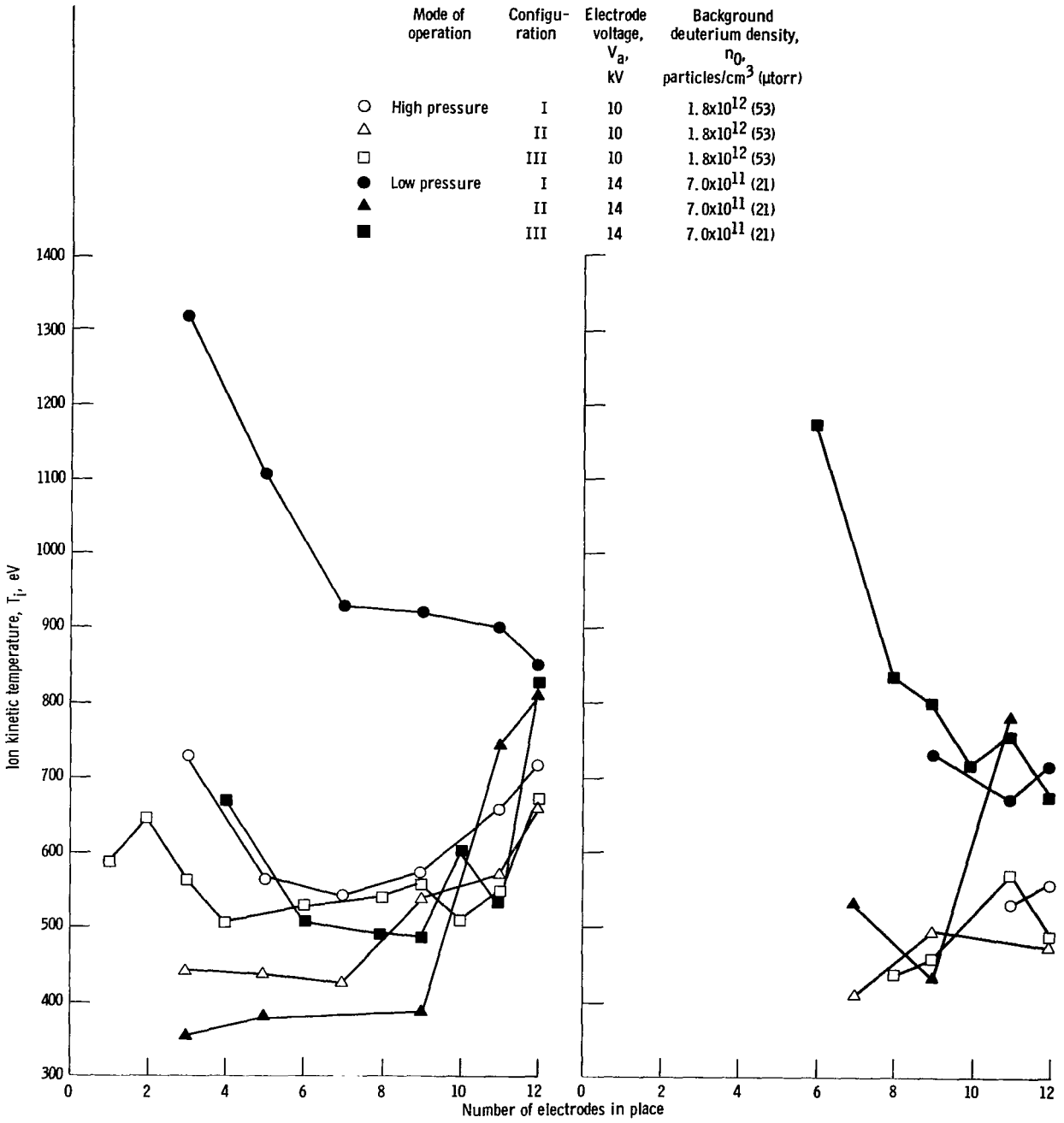

(a) Positive electrode polarity.

(b) Negative electrode polarity.

Figure 22. - Ion kinetic temperature as function of electrode ring configurations listed in table I for two background deuterium densities. Maximum magnetic field strength, B_{max}, 2.4 teslas.

EFFECTS OF PLASMA IMPURITY FRACTION

There has recently been concern about the effects of impurities on plasma characteristics and on the interpretation of raw data from diagnostic instruments, particularly charge-exchange neutral particle detectors. The charge-exchange neutral detector used to measure the ion energy distribution function in this experiment is a duplicate of that developed by Valckx at Fontenay-aux-Roses (ref. 23) and is a 90°-curved-plate electrostatic energy analyzer. This class of instruments has the disadvantage that it is incapable of distinguishing between species of different masses at a given energy. Thus, data that supposedly measure the distribution function of atomic or molecular deuterium may be contaminated with impurity ions of higher atomic weight. Stirling (ref. 24) has shown that the charge-exchange neutral flux from the "Burnout" device at the Oak Ridge National Laboratory was contaminated to a significant extent by charge-exchange neutrals from impurities in the plasma. These impurities were detected by putting the flux of reionized energetic particles successively through two instruments, a parallel-plate electrostatic analyzer similar to that used in this experiment, followed by a magnetic momentum analyzer, to separate equal-energy ions of different masses. It was found that most of the impurities were of a type to be expected from the heated electrodes that were in direct contact with that plasma. A similar analysis was performed with the hot ion plasma in the SUMMA facility (ref. 25), and several energetic impurities were identified that could contaminate the ion energy distribution function measured without mass analysis.

The procedure adopted to assess the possible effect of impurities on the number density and ion kinetic temperature was to deliberately introduce into the plasma a controlled amount of an impurity. These included helium, nitrogen, neon, and argon. This impurity fraction was increased until significant effects on the density or the nature of the ion energy distribution function became apparent.

The measurement of ion kinetic temperature and number density as a function of impurity fraction required from 30 to 45 minutes for each impurity investigated. It was not possible to hold the ion kinetic temperature or the number density absolutely constant for that length of time. Figures 23(a) and (b) show the measured ion kinetic temperature and number density as a function of time, under conditions when no impurities were introduced into the plasma but for which the plasma was held at the most constant possible conditions. The ion kinetic temperature varied up to 7 percent during this length of time, and the plasma number density varied by about 13 percent.

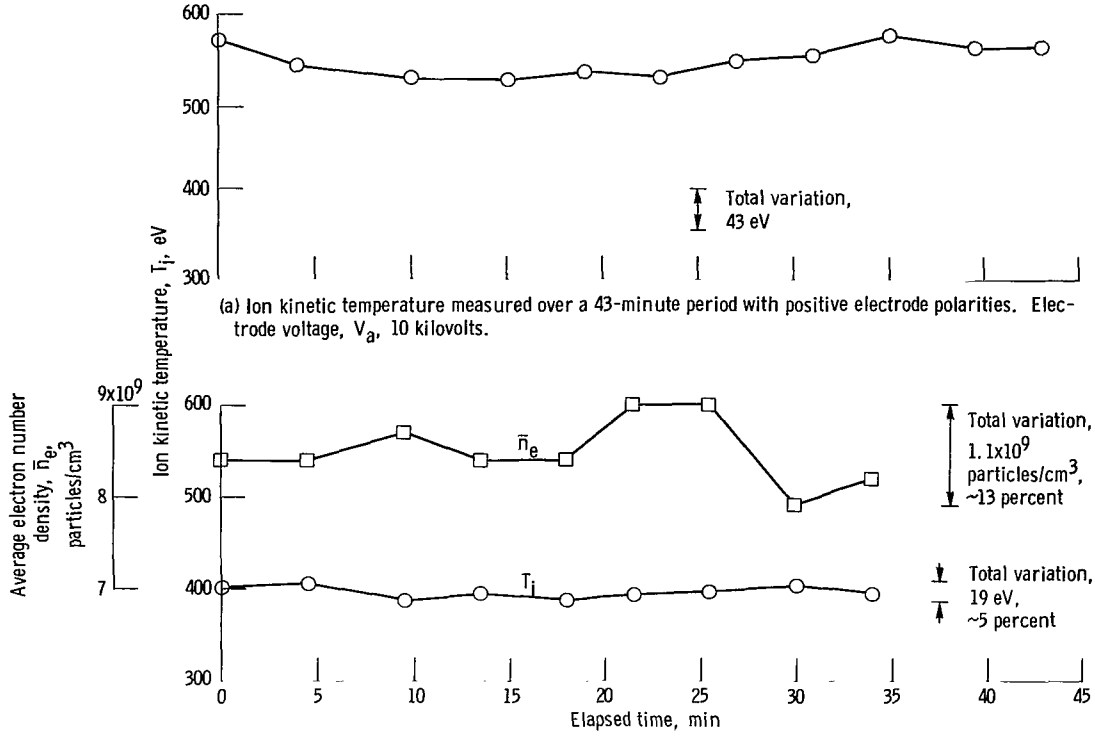

(a) Ion kinetic temperature measured over a 43-minute period with positive electrode polarities. Electrode voltage, V_a, 10 kilovolts.

(b) Ion kinetic temperatures and electron number densities measured over a 34-minute period with negative electrode polarities. Electrode voltage, V_a, 8 kilovolts.

Figure 23. - Measured ion kinetic temperature and number density as function of time with operating conditions held as constant as possible. Background deuterium density, n_0, 1.8×10^{12} particles/cm^3 (53 μtorr); maximum magnetic field strength, B_{max}, 2.4 teslas.

Background Impurities in Plasma

The composition of the neutral background gas in the vacuum tank was monitored with a quadrupole mass spectrometer before, during, and after data were taken. The total background density, read on a well-baked-out ion gage, was typically about 3.6×10^9 particles/cm^3 (0.11 μtorr). The principal impurity was nitrogen, with some oxygen in the proportion found in air. There were no significant leaks in the liquid-helium system or in the liquid-nitrogen circuits inside the vacuum tank.

An attempt was made to identify impurity lines in the plasma by sweeping the optical region of the spectrum with a 1.5-meter Fastie-Ebert optical spectrometer that was used in spectroscopic investigations (refs. 1 and 2). No impurity line emission could be detected under any conditions of plasma operation accessible to the apparatus at the time these measurements were made (private communication with R. W. Richardson). The

much smaller level of background impurities in the bumpy-torus plasma, relative to the ion magnetron discharges reported in references 24 and 25, very probably resulted from the fact that the latter plasmas have carbon (ref. 24) or tungsten and copper (ref. 25) electrodes in direct contact with the plasma along magnetic field lines, whereas the bumpy-torus plasma has cooled electrode rings outside the plasma boundary and separated from it by electrode sheaths.

Effect of Impurity Fraction on Ion Kinetic Temperature

Controlled amounts of helium, nitrogen, neon, and argon were bled into the vacuum tank to form a plasma in which these impurities had varying concentrations. The relative concentrations were determined by measuring the height of each species on a quadrupole mass spectrometer and multiplying these peak heights by the gage factor appropriate for that species (ref. 26). The ion kinetic temperature and electron number density were measured under otherwise constant conditions. The ion kinetic temperature is plotted as a function of the percentage of impurity in figure 24 for positive potentials on the midplane electrode rings. The ion kinetic temperatures are not affected until the impurity concentrations exceed 10 percent. The ion kinetic temperature is shown as a function of the impurity concentration for the same four gases in figure 25 for negative potentials on the midplane electrodes. For both polarities, the partial pressure of deuterium remained constant and the total pressure rose slightly as the partial pressure of the impurities reached high levels.

The ion kinetic temperature was virtually independent of the neutral impurity fraction for all four gases for both electrode ring polarities up to concentrations of 10 percent. For negative polarities, the ion kinetic temperature did not change significantly even for concentrations approaching 100 percent. The nature of the ion energy distribution function did not change as the impurity concentration increased for either polarity, implying that impurities are not responsible for the non-Maxwellian velocity distributions sometimes observed under certain operating conditions. The fact that the energy distribution functions are not seriously perturbed by impurities implies that the charge-exchange cross sections for both the original impurity charge exchange and/or reionization in the nitrogen gas cell must be substantially lower than for the same atomic processes in deuterium gas. Unfortunately, these impurity charge-exchange and reionization cross sections are not well known, but the present evidence seems to indicate that they are small.

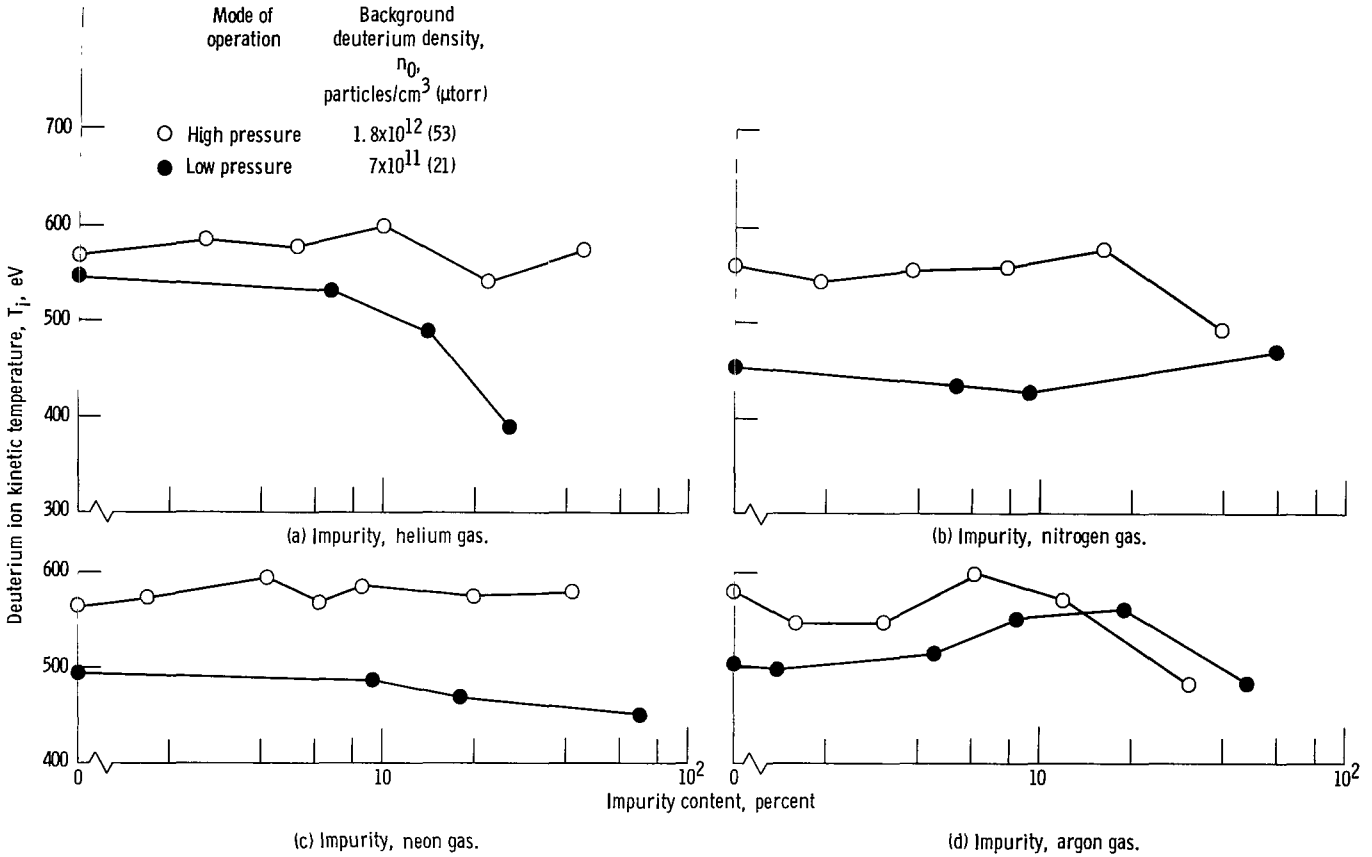

Figure 24. - Ion kinetic temperature as function of percentage of impurity for both modes of operation and positive electrode polarities. Background gas, deuterium; maximum magnetic field strength, B_{max}, 2.4 teslas; electrode voltage, V_a, 10 kilovolts.

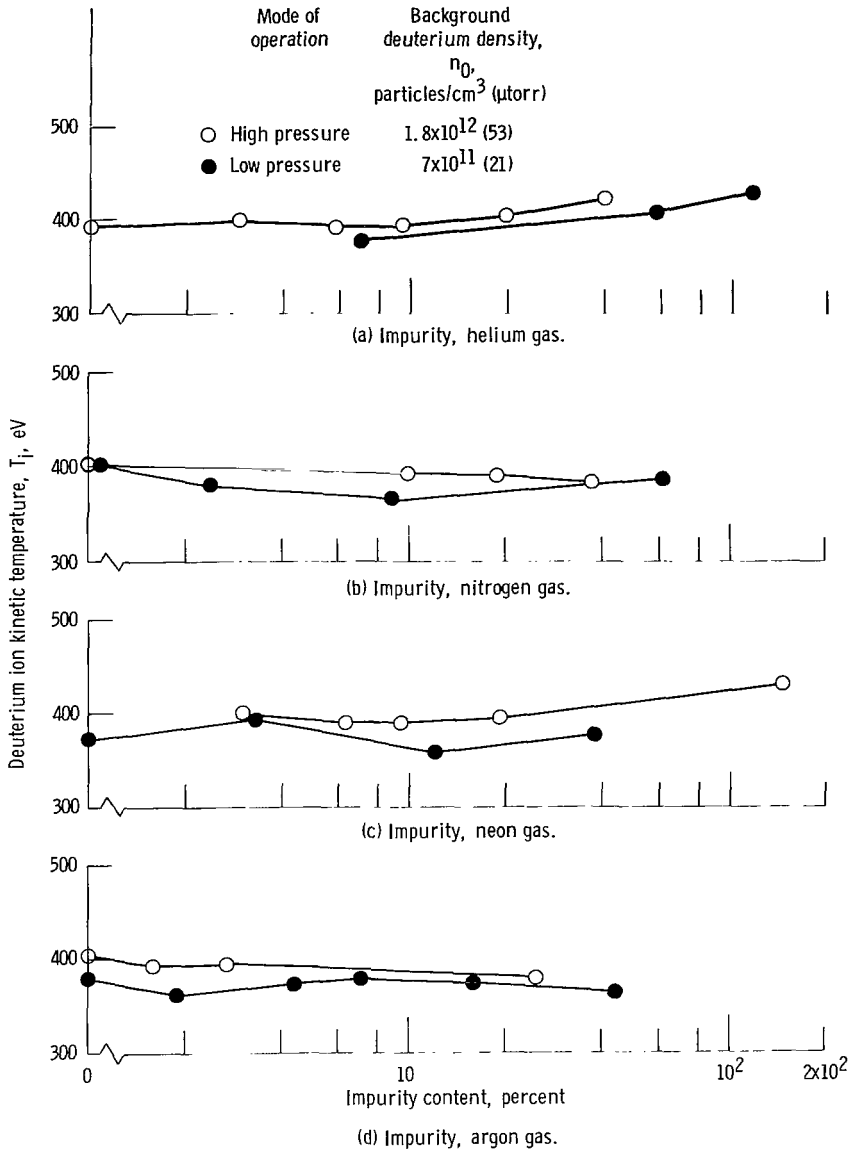

Figure 25. - Ion kinetic temperature as function of percentage of impurity for both modes of operation and negative electrode polarities. Background gas, deuterium; maximum magnetic field strength, B_{max}, 2.4 teslas.

Effect of Impurity Fraction on Electron Number Density

The average electron number density was measured with a microwave interferometer at the same time that the impurity fractions were being varied for the measurement of ion kinetic temperature. Figure 26 shows the average electron number density as a function of the impurity fraction for both modes of operation and for positive potentials on the midplane electrode rings. There is no significant effect for impurity concentra-

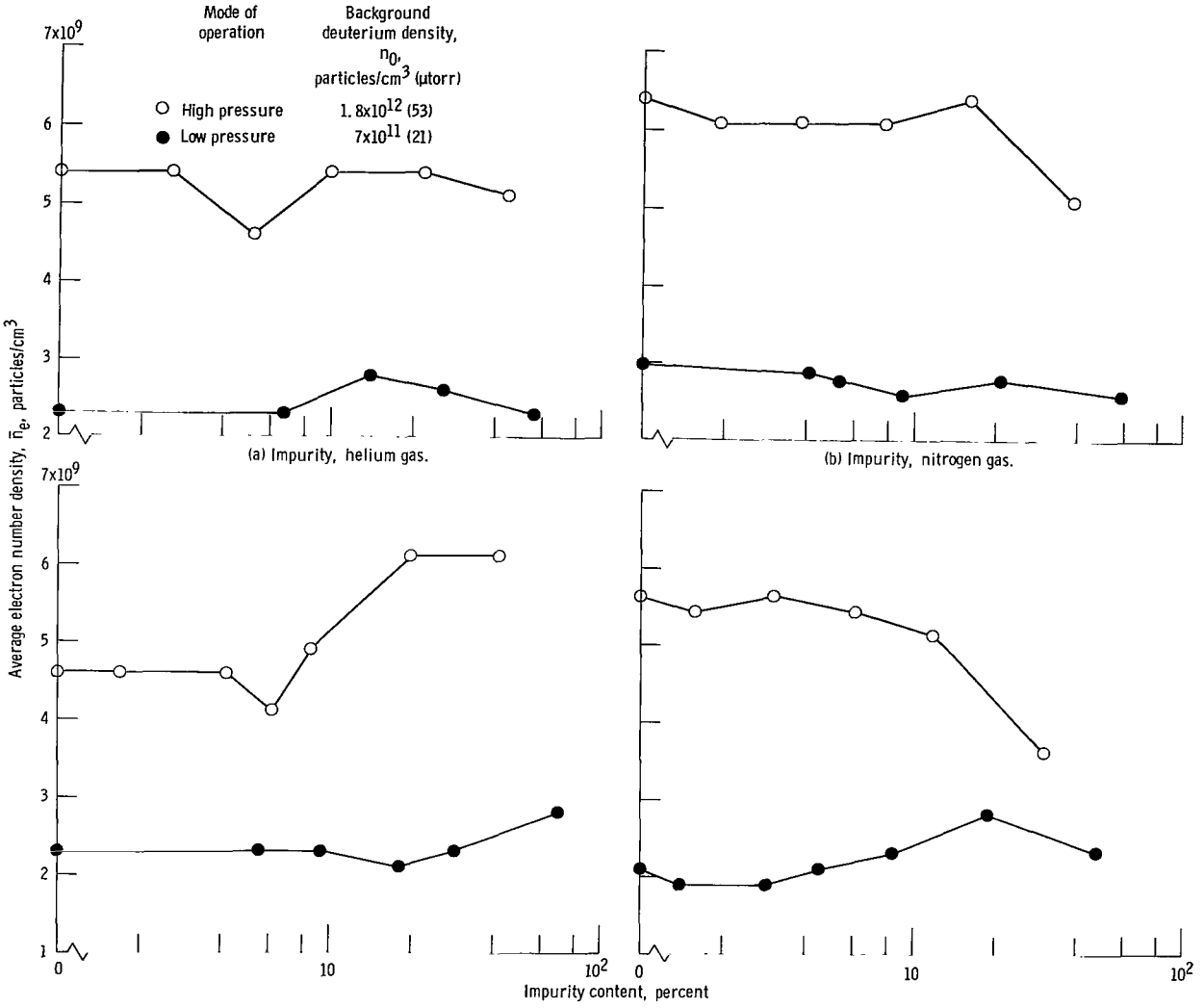

Figure 26. - Average electron number density as function of impurity concentration for both modes of operation and positive electrode polarities. Background gas, deuterium; maximum magnetic field strength, B_{max}, 2.4 teslas; electrode voltage, V_a, 10 kilovolts.

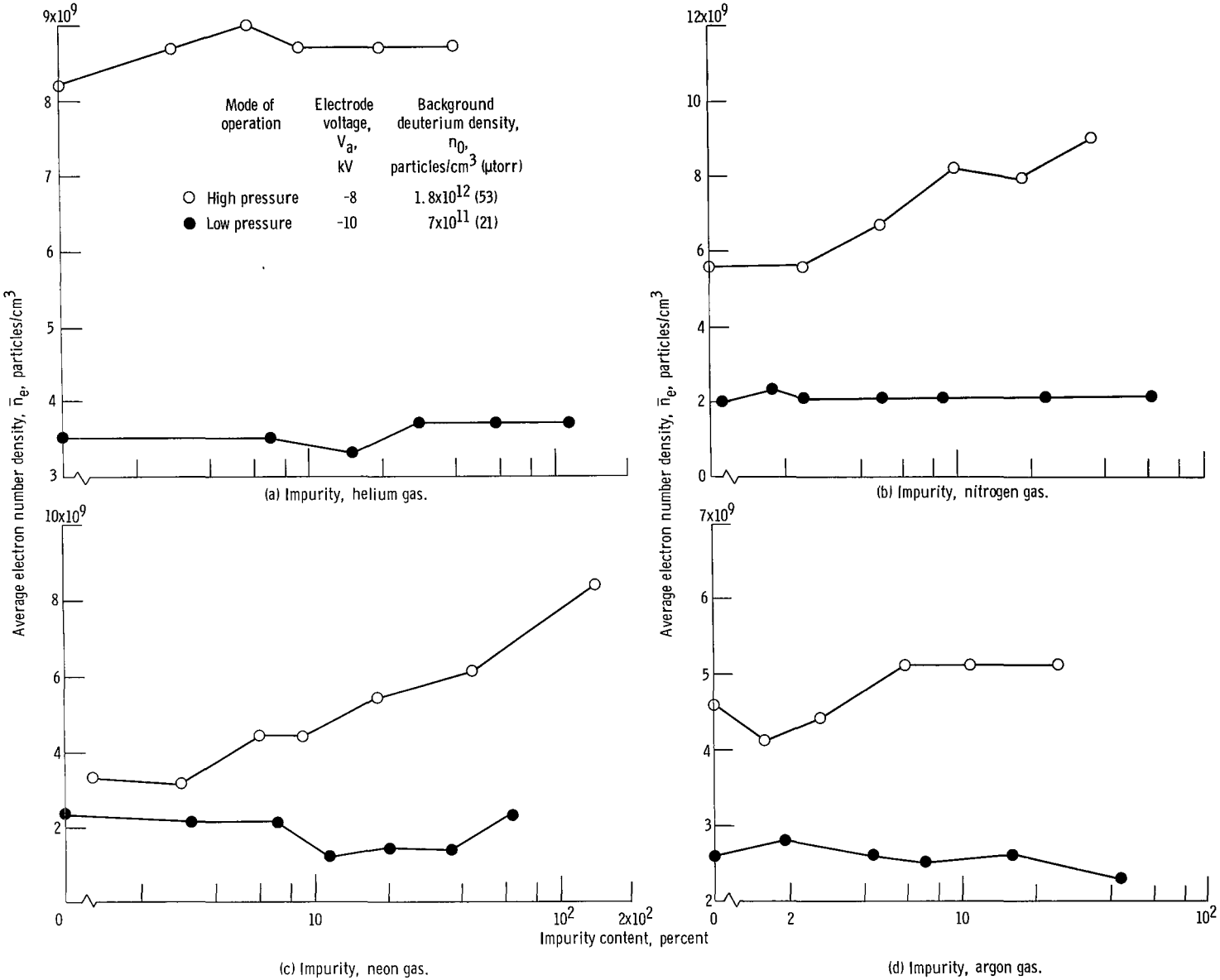

Figure 27. - Average electron number density as function of impurity concentration for both modes of operation and negative electrode polarities. Background gas, deuterium; maximum magnetic field strength, B_{max}, 2.4 teslas.

tions below 10 percent. The same operating conditions are shown in figure 27 for negative polarities on the midplane electrode rings. The addition of impurities did not affect the electron number density in the low-pressure mode of operation. In the high-pressure mode, the density increased with impurity fraction in figures 27(b) and (c) because the plasma was operating in a bistable manner between the densities exhibited in figures 27(a) and (d) when increasing amounts of nitrogen and neon impurities were added.

PLASMA CURRENT-VOLTAGE CHARACTERISTICS

A limited number of current-voltage curves for deuterium and helium gas were published in references 1, 2, and 11. These data were taken under conditions for which the midplane electrode rings were alined by eye, and they could have been displaced radially with respect to the magnetic axis by as much as 1.5 centimeters. They may have been displaced vertically or axially from the midplane by a similar amount. The data presented in figure 19 show that the current-voltage curves depend strongly on their vertical position and on any displacement from the midplane. Electrode alinement devices have been installed in the vacuum tank and have been positioned at the location shown in figures 4 and 6 for all data presented in this report. These alinement devices make it possible to aline all 12 midplane electrode rings within about 3 millimeters of the same position relative to the magnetic axis and the midplane of the adjacent coil pair. They also make it possible to remove and replace an electrode ring while the tank is under vacuum, without its replacement affecting its relative alinement.

Current-voltage curves were taken with 12 electrode rings at a constant maximum magnetic field of 2.4 teslas in deuterium gas, for a positive polarity on the electrode rings and for eight background pressures of neutral deuterium gas. These current-voltage curves are shown in figure 28. Current-voltage curves for negative midplane electrode rings and for the same conditions as figure 28 are shown in figure 29.

If all conditions but polarity are the same, there is a tendency for the plasma to draw more current when the electrode rings are negative than when they are positive. The current-voltage curves in figures 28 and 29 differ only in detail from those published in references 1, 2, and 11. The misalinements that possibly existed in previous work have a lesser effect on the current-voltage curves than the polarity of the midplane electrode rings.

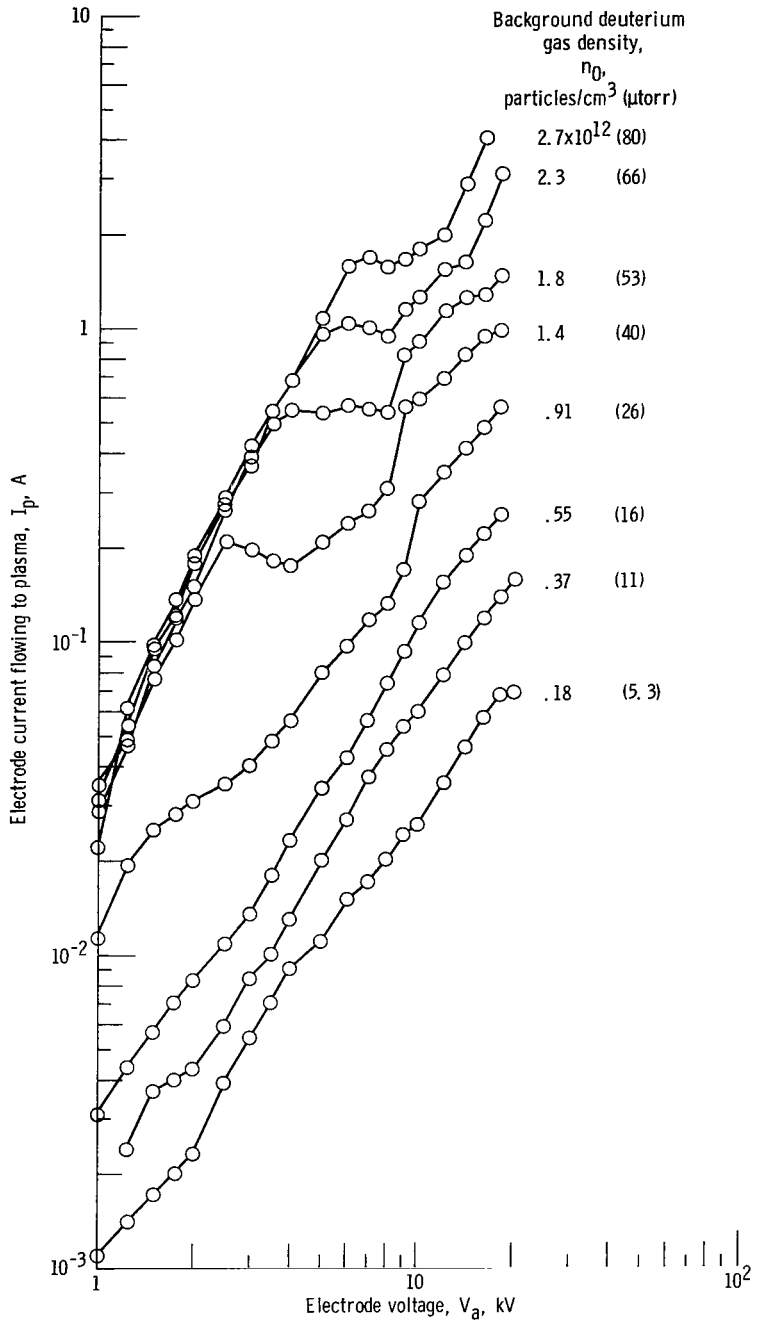

Figure 28. - Current-voltage curves for eight different background pressures of deuterium gas at a maximum magnetic field strength B_{max} of 2.4 teslas and positive polarities on 12 midplane electrode rings.

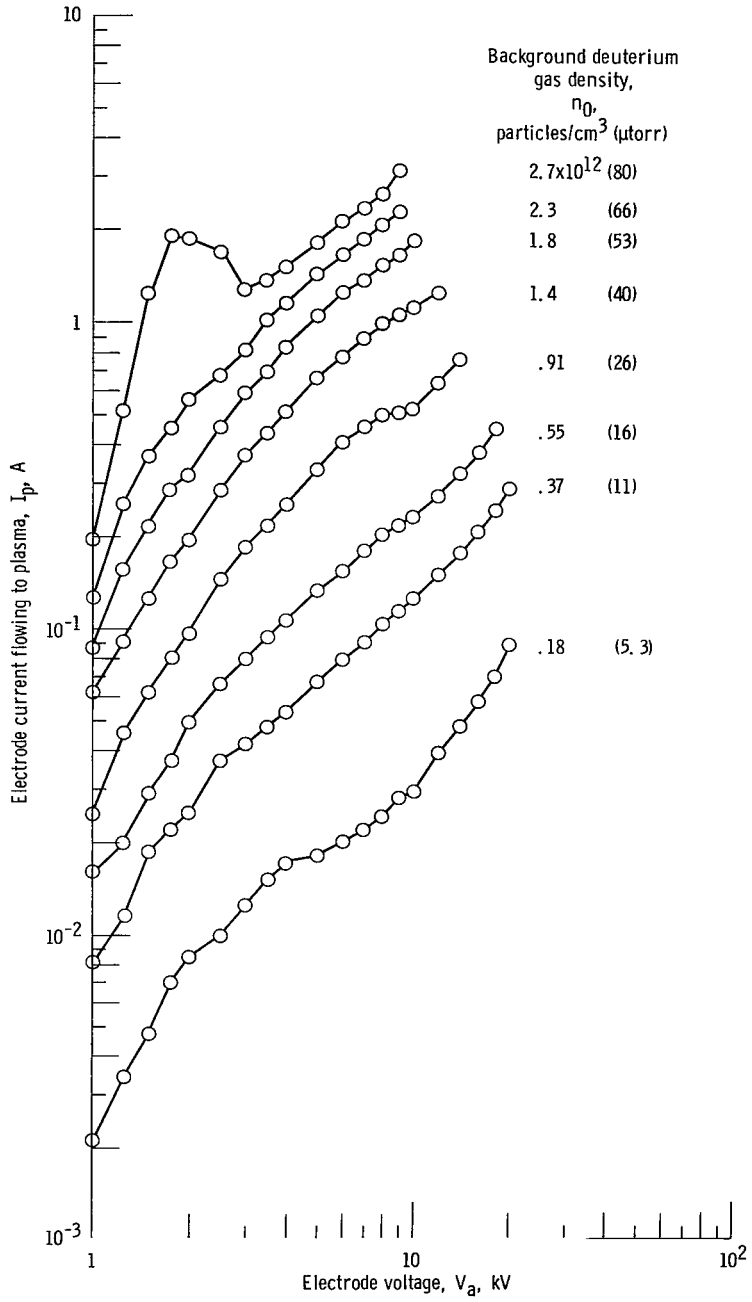

Figure 29. - Current-voltage curves for eight different background pressures of deuterium gas at a maximum magnetic field strength B_{max} of 2.4 teslas and negative polarities on 12 midplane electrode rings.

EFFECTS OF ELECTRIC FIELD ON PLASMA CONTAINMENT

As was pointed out in the INTRODUCTION, a characteristic feature of this experiment is the biasing of the entire toroidal ring of plasma to high potentials, either positive or negative, in the manner that has been documented previously in reference 11 by data from floating Langmuir probes inserted in the plasma. In that reference, it was shown that the toroidal ring of plasma assumes floating potentials, the maximum values of which are comparable to the potentials on the midplane electrode rings. These applied potentials can reach values of 50 kilovolts and give rise to radial electric fields between the plasma and the grounded magnet dewars of 1 to 10 kV/cm.

In this section, some preliminary evidence is presented relating to the effects on plasma containment of the radial electric fields; under what conditions these effects are beneficial; and finally, in what direction future research should be directed in order to maximize the beneficial effects of these radial electric fields.

Toroidicity of Electric Field

The first-order effect of the radial electric fields between the plasma torus and the grounded walls is to raise the ions and electrons to high energies by $E \times B$ drift. The existence of high ion energies and their subsequent thermalization to Maxwellian distributions have been documented in references 7 to 11. The nature of the electric field distribution can be understood with the help of figure 30, which shows the magnetic field lines associated with the toroidal magnetic field and the approximate location of the confined plasma in a typical sector. The location of the electrode ring shown in figure 30 is at the position along the major radius of the torus used for all investigations covered in this report. The first-order radial electric field extends from the plasma interior to the grounded magnet dewars that surround the confined plasma. It is this electric field, along the minor radius of the toroidal plasma, that is responsible for raising the ions to high energies by $E \times B$ drift.

The plasma is toroidal, and there is a significant second-order effect on plasma containment because of the toroidicity of the electric field. If the electrode rings were lined up with the geometric axis of the toroidal volume enclosed by the magnet dewars, the very fact that the plasma column is bent into a torus would result in slightly higher electric fields on the inside major radius than on the outside radius of the plasma. This toroidicity would tend to produce a stronger radial electric field on the inside circumference of the plasma than on the outside circumference. A particle drifting around the minor circumference of the plasma would see a net electric field pointing radially inward or outward along the major radius of the torus. Such a second-order electric field along the major radius of the torus can also arise as a result of the misalinement of the

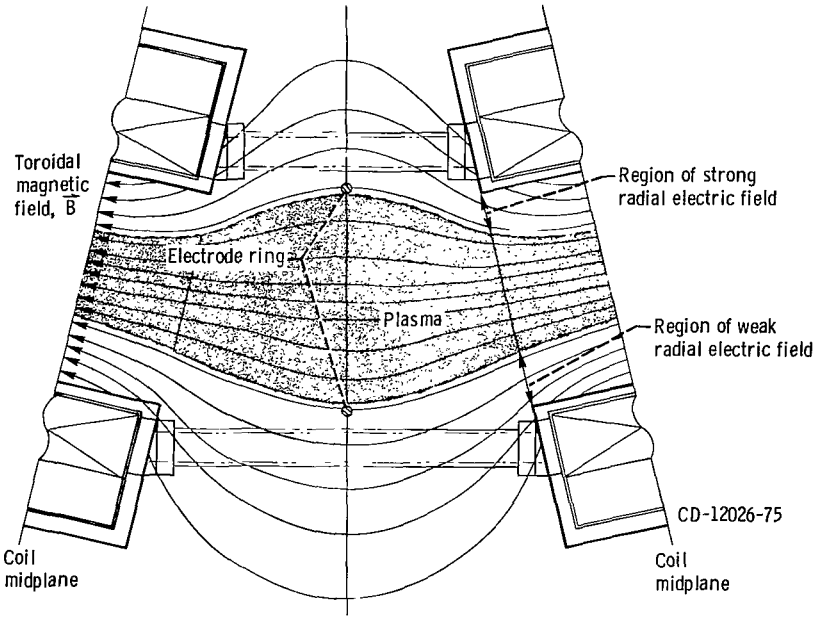

Figure 30. - Cross section of bumpy-torus plasma in equatorial plane, showing plasma and electrode ring locations used in investigations in this report.

electrode rings off the geometrical axis of the toroidal volume, as is the case in the present experiments depicted in figure 30. For the present experiments, the plasma is displaced radially inward to better conform to the magnetic field drift surfaces. As a result, the inner circumference of the plasma is closer to the magnet dewars than is the outer circumference.

The situation shown in figure 30 gives rise to a net electric field pointing inward along the major radius of the torus (for positive polarities), both because of the toroidicity of the electric field and also as a result of the radial displacement of the plasma toward the vertical axis of the toroidal array. As a particle drifts around the minor circumference of the plasma, it will experience this net radial electric field, and particles of both signs will then drift to the top of the plasma for positive electrode polarities. With negative electrode polarities, the net radial electric fields are such that the drifts will be to the bottom of the torus. Such behavior has been observed qualitatively, in that the plasma appears to be more luminous and to have a sharper boundary on the top surface of the confinement volume when positive electrodes are used. The situation is reversed, with the plasma appearing to sink to the bottom of the containment volume, when negative polarities are used.

Probably the easiest way of eliminating the second-order electric field drifts due to the toroidicity and radial misalinement of the plasma column is to move the midplane electrode rings radially outward, until the net electric field experienced by a particle

drifting around the minor circumference of the plasma is zero. This can best be done through a trial-and-error process of moving the electrode rings radially outward in incremental steps and measuring the electron number densities and containment times until an optimum value is reached. Such a procedure is planned for a future series of investigations.

Polarity of Electric Field

It was anticipated that the strong electric fields acting along the minor radius of the plasma would not only heat the plasma to high energies by $E \times B$ drift, but might also have a beneficial effect on plasma containment. A plasma containment effect would be expected because either the ions or the electrons would be in an electrostatic potential well, depending on the polarity of the midplane electrode rings and the consequent plasma bias. By applying positive potentials to the electrode rings, the entire plasma can be made positive and an electrostatic potential well for electrons. However, one must then expect that the ions will be transported radially outward toward the walls. Since the ions are hotter than the electrons and more mobile, the ion loss rate would be substantial.

With the midplane electrode rings negative, the ions are in a potential well and may be transported radially inward into the center of the plasma by the electric fields. Any stochastic process occurring in the plasma would tend to infuse ions into the center of the plasma. However, the electrons are on an electrostatic potential hill and tend to be transported radially outward toward the walls. Since the magnetic field is extremely strong, the electrons must suffer many collisions before they can migrate from the center of the plasma to the outside. We might then anticipate that negative polarities and electric fields pointing radially inward would have a beneficial net effect on containment.

Some preliminary paired comparison data were taken on the relative effects of positive and negative polarities on plasma containment, and these data are plotted in figures 31 and 32. These figures show the confinement time in milliseconds, calculated from equation (2), plotted against the average particle number density measured with the microwave interferometer. The average particle number density was that measured with the microwave interferometer, and the plasma volume was 82 liters. Figures 31 and 32 are for five different background pressures of neutral deuterium gas, with only electrodes 5 and 6 in place, and for a maximum magnetic field of 2.4 teslas.

There are two principal comparisons that might be considered relevant to assessing the effect of positive and negative polarities on containment. One, illustrated in figure 31 and table II, is for equal voltages to be applied to the midplane electrode rings, with the currents flowing to the electrode rings assuming whatever values are appropri-

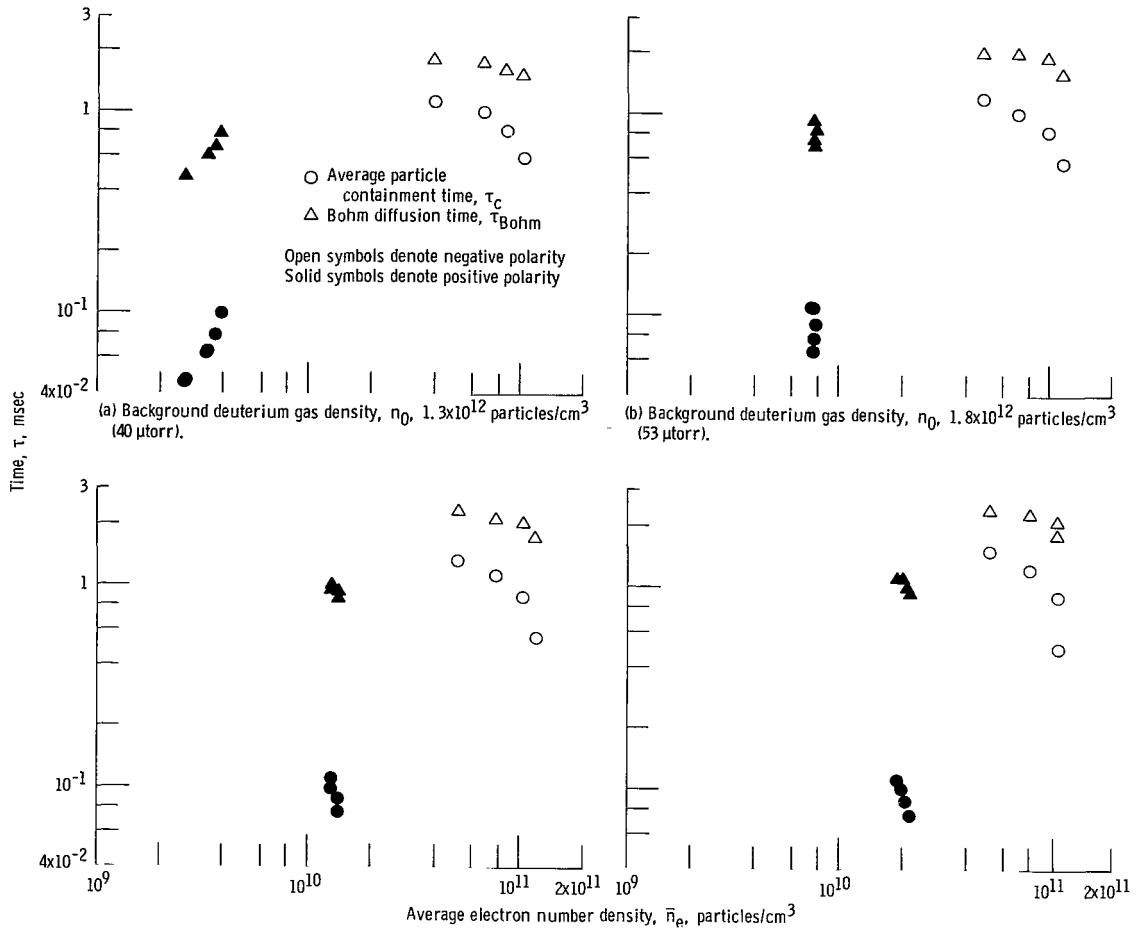

(a) Background deuterium gas density, n_0, $1.3x10^{12}$ particles/cm^3 (40 μtorr).

(b) Background deuterium gas density, n_0, $1.8x10^{12}$ particles/cm^3 (53 μtorr).

(c) Background deuterium gas density, n_0, $2.2x10^{12}$ particles/cm^3 (66 μtorr).

(d) Background deuterium gas densities, n_0, $2.6x10^{12}$ particles/cm^3 (80 μtorr).

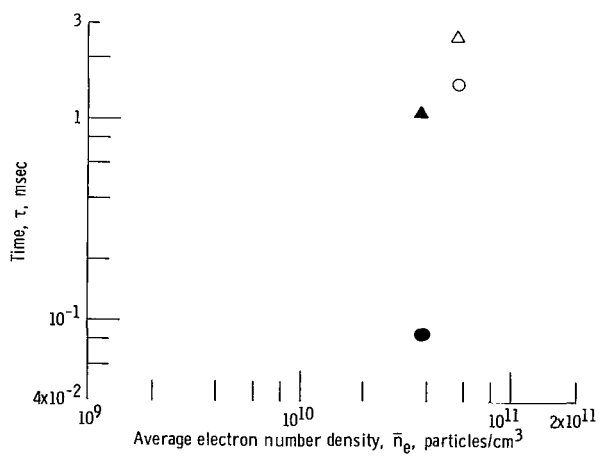

(e) Background deuterium gas density, n_0, $3.5x10^{12}$ particles/cm^3 (106 μtorr).

Figure 31. - Plasma containment time calculated from equation (2) as function of average electron number density measured with microwave interferometer, for runs with positive and negative electrode polarities and equal electrode voltages. Electrodes 5 and 6 in place; maximum magnetic field strength, B_{max}, 2.4 teslas. (The raw data are shown on table II.)

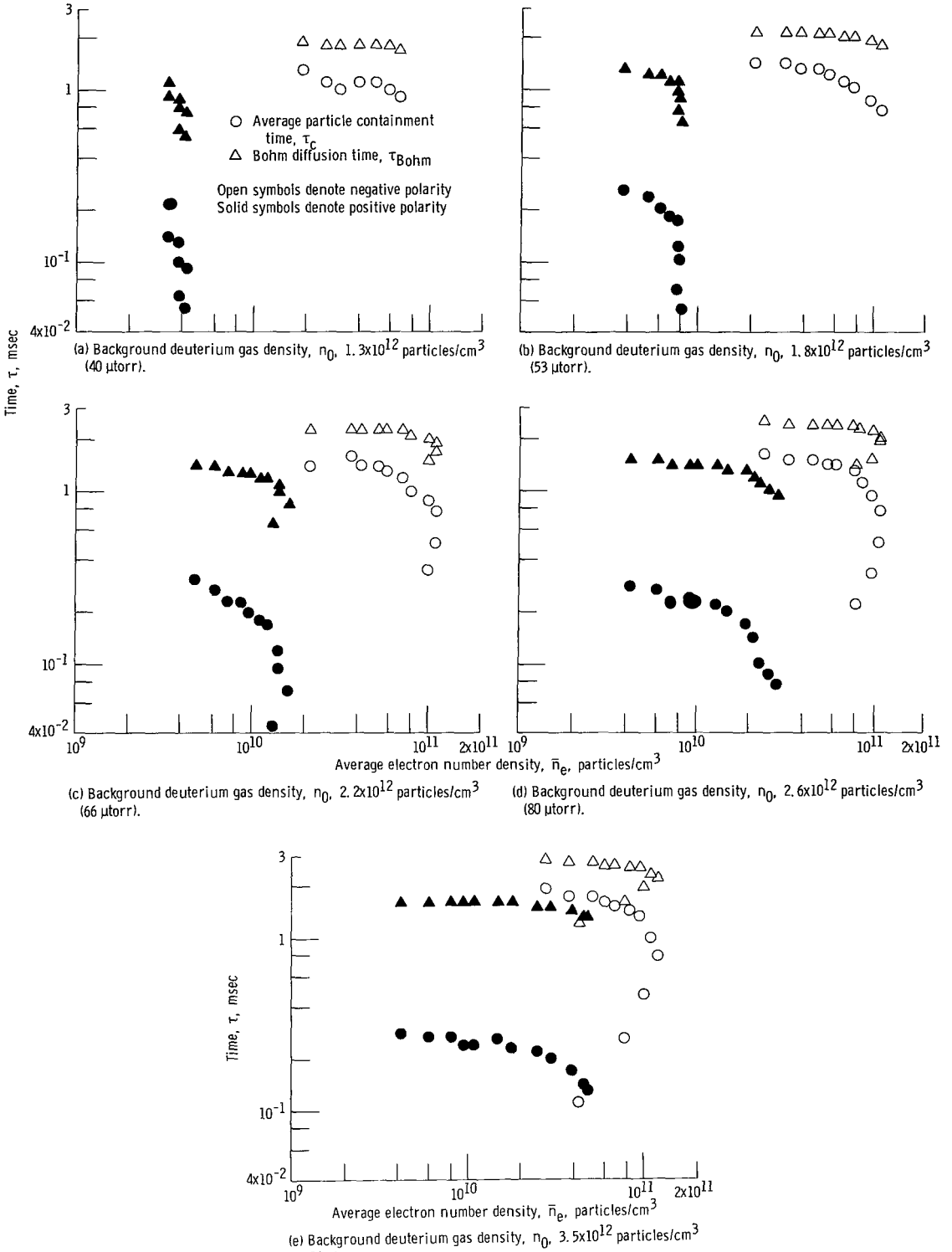

(a) Background deuterium gas density, n_0, 1.3x10^{12} particles/cm^3 (40 μtorr).

(b) Background deuterium gas density, n_0, 1.8x10^{12} particles/cm^3 (53 μtorr).

(c) Background deuterium gas density, n_0, 2.2x10^{12} particles/cm^3 (66 μtorr).

(d) Background deuterium gas density, n_0, 2.6x10^{12} particles/cm^3 (80 μtorr).

(e) Background deuterium gas density, n_0, 3.5x10^{12} particles/cm^3 (106 μtorr).

Figure 32. - Plasma containment time calculated from equation (2) as function of average electron number density measured with microwave interferometer, for runs with positive and negative electrode polarities and equal electrode currents. Electrodes 5 and 6 in place; maximum magnetic field strength, B_{max}, 2.4 teslas. (The raw data are shown in table II.)

TABLE II. - DATA TAKEN AT FIVE PRESSURES OF NEUTRAL DEUTERIUM GAS WITH B_{max} = 2.4 TESLA AND ELECTRODES IN SECTORS 5 AND 6 - PAIRED COMPARISON WITH EQUAL VOLTAGES AT OPPOSITE POLARITIES

Vacuum tank pressure		Electrode voltage, V_a, kV	Positive polarity					Negative polarity				
Particles/cm^3	μtorr		Total current, I_p, A	Average electron number density, $\bar{n}_e$, particles per cm^3	Particle containment time, τ_c, msec	Calculated electron temperature, T_e, eV	Equivalent Bohm time, τ_{Bohm}, msec	Total current, I_p, A	Average electron number density, $\bar{n}_e$, particles per cm^3	Particle containment time, τ_c, msec	Calculated electron temperature, T_e, eV	Equivalent Bohm time, τ_{Bohm}, msec
1.3×10^{12}	40	1	0.221	0.38×10^{10}	0.23	7.6	1.1	-----	---------	----	---	---
		1.5	.348	.38	.14	9.4	.91	-----	---------	----	---	---
		2	.483	.38	.10	11	.78	0.486	4.0×10^{10}	1.1	4.8	1.8
		2.5	.607	.36	.078	12.8	.67	.897	6.7	.97	4.9	1.7
		3	.670	.33	.065	14	.61	1.47	8.6	.77	5.4	1.6
		3.5	.703	.26	.047	18	.48	2.37	10.5	.58	5.8	1.5
1.8×10^{12}	53	1	0.381	0.61×10^{10}	0.22	7.1	1.2	-----	---------	----	---	---
		1.5	.670	.74	.14	8.4	1.0	-----	---------	----	---	---
		2	.936	.76	.11	9.3	.92	0.510	4.8×10^{10}	1.2	4.2	2.0
		2.5	1.14	.78	.090	10.2	.84	.936	7.1	1.0	4.3	2.0
		3	1.36	.76	.073	11.2	.76	1.60	9.8	.81	4.6	1.9
		3.5	1.50	.76	.067	11.8	.73	2.69	11.4	.56	5.4	1.6
2.2×10^{12}	66	1	0.659	0.95×10^{10}	0.19	6.9	1.2	-----	---------	----	---	---
		1.5	1.15	1.2	.14	7.6	1.1	-----	---------	----	---	---
		2	1.52	1.3	.11	8.4	1.0	0.524	5.2×10^{10}	1.3	3.8	2.3
		2.5	1.83	1.3	.096	8.8	.97	.926	7.8	1.1	4.0	2.1
		3	2.19	1.4	.086	9.3	.92	1.60	10.5	.86	4.2	2.0
		3.5	2.55	1.4	.074	10	.86	2.83	12	.54	5.0	1.7
2.6×10^{12}	80	1	0.976	1.4×10^{10}	0.19	6.4	1.3	-----	---------	----	---	---
		1.5	1.74	1.8	.14	7.2	1.2	-----	---------	----	---	---
		2	2.26	1.9	.11	7.8	1.1	0.473	5.2×10^{10}	1.5	3.5	2.4
		2.5	2.67	2.0	.10	8.1	1.1	.905	8.1	1.2	3.7	2.3
		3	3.29	2.1	.086	8.6	1.0	1.62	11	.88	4.0	2.1
		3.5	4.0	2.2	.073	9.3	.92	3.10	11	.49	4.7	1.8
3.5×10^{12}	106	1	2.66	3.4×10^{10}	0.17	6.2	1.4	-----	---------	----	---	---
		1.5	4.39	4.2	.13	6.8	1.3	-----	---------	----	---	---
		2	5.85	3.8	.086	7.7	1.1	0.487	5.7×10^{10}	1.5	3.3	2.6
		2.5	-----	---------	-----	----	----	.883	8.8	1.3	3.4	---
		3	-----	---------	-----	----	----	1.53	11	.99	3.6	---
		3.5	-----	---------	-----	----	----	3.19	10	.41	4.6	---

TABLE III. - DATA TAKEN AT FIVE PRESSURES OF NEUTRAL DEUTERIUM GAS WITH B_{max} = 2.4 TESLAS AND ELECTRODES IN SECTORS 5 AND 6 - PAIRED COMPARISON WITH EQUAL CURRENTS FLOWING TO ELECTRODES, AT OPPOSITE ELECTRODE POLARITIES

Vacuum tank pressure		Electrode current, I_p, A	Positive polarity					Negative polarity				
Particles/cm^3	μtorr		Electrode voltage, V_a, kV	Average electron number density, $\bar{n}_e$, particles per cm^3	Particle containment time, τ_c, msec	Calculated electron temperature, T_e, eV	Equivalent Bohm time, τ_{Bohm}, msec	Electrode voltage, V_a, kV	Average electron number, density, $\bar{n}_e$, particles per cm^3	Particle containment time, τ_c, msec	Calculated electron temperature, T_e, eV	Equivalent Bohm time, τ_{Bohm}, msec
1.3×10^{12}	40	0.2	0.88	0.33×10^{10}	0.22	7.8	1.1	1.90	1.9×10^{10}	1.3	4.4	1.9
		.3	1.12	.33	.14	9.4	.91	1.96	2.6	1.1	4.7	1.8
		.4	1.47	.38	.13	9.7	.88	1.97	3.1	1.0	4.8	↓
		.5	1.86	.38	.10	11	.78	2.05	4.0	1.1	4.7	
		.6	2.23	.42	.092	11.6	.74	2.17	5.0	1.1	4.7	
		.8	3.08	.38	.063	14.4	.59	2.36	5.9	1.0	4.8	↓
		1.0	5.15	.41	.054	16	.54	2.57	6.7	.87	5.1	1.7
1.8×10^{12}	53	0.2	0.69	0.38×10^{10}	0.26	6.8	1.3	1.76	2.1×10^{10}	1.4	4.0	2.1
		.3	.86	.52	.23	7.0	1.2	1.74	3.1	1.4	4.0	↓
		.4	1.01	.61	.20	7.3	1.2	1.84	3.8	1.3	4.1	
		.5	1.16	.69	.18	7.6	1.1	2.03	4.8	1.3	4.1	
		.6	1.31	.76	.17	7.8	1.1	2.15	5.5	1.2	4.1	↓
		.8	1.73	.76	.12	9.0	.95	2.34	6.7	1.1	4.2	2.0
		1.0	2.12	.78	.10	9.6	.89	2.58	7.6	1.0	4.3	2.0
		1.5	3.28	.76	.067	11.8	.73	2.96	9.5	.83	4.6	1.9
		2.0	5.39	.81	.052	13.5	.63	3.23	11	.73	4.8	1.8
2.2×10^{12}	66	0.2	0.59	0.47×10^{10}	0.31	6.0	1.4	1.71	2.1×10^{10}	1.4	3.8	2.3
		.3	.66	.61	.27	6.2	1.4	1.73	3.6	1.6	3.7	↓
		.4	.73	.72	.23	6.5	1.3	1.83	4.1	1.4	3.8	
		.5	.81	.86	.23	6.5	1.3	2.02	5.2	1.4	3.8	
		.6	.89	.95	.20	6.8	1.3	2.13	5.7	1.3	3.8	
		.8	1.04	1.1	.18	7.0	1.2	2.40	7.1	1.2	3.9	↓
		1.0	1.23	1.2	.17	7.2	1.2	2.55	7.8	1.0	4.1	2.1
		1.5	1.77	1.4	.12	8.1	1.1	2.97	10	.87	4.2	2.0
		2.0	2.48	1.4	.095	9.0	1.0	3.24	11	.76	4.4	1.9
		3.0	3.94	1.6	.070	10.2	.84	3.55	11	.50	5.1	1.7
		4.0	6.50	1.3	.044	13	.66	3.75	10	.35	5.8	1.5
2.6×10^{12}	80	0.2	0.53	0.42×10^{10}	0.28	5.8	1.5	1.71	2.4×10^{10}	1.6	3.4	2.5
		.3	.59	.60	.27	5.8	1.5	1.72	3.3	1.5	3.5	2.4
		.4	.65	.72	.23	6.1	1.4	1.85	4.5	1.5	3.5	↓
		.5	.69	.91	.24	6.0	↓	2.03	5.5	1.4	3.6	
		.6	.74	1.0	.23	6.1		2.14	6.2	1.4	3.6	
		.8	.82	1.3	.22	6.2		2.42	7.8	1.3	3.6	↓
		1.0	.88	1.5	.20	6.4	1.3	2.60	8.6	1.1	3.8	2.3
		1.5	1.12	1.9	.17	6.7	1.3	2.97	10	.92	3.9	2.2
		2	1.43	2.1	.14	7.2	1.2	3.22	11	.76	4.2	2.0
		3	2.32	2.3	.10	8.1	1.1	3.49	11	.50	4.6	1.9
		4	2.67	2.6	.086	8.6	1.0	3.70	10	.33	5.6	1.5
		5	3.24	2.9	.076	9.1	.94	3.84	8.1	.22	6.2	1.4
3.5×10^{12}	106	0.2	0.48	0.42×10^{10}	0.28	5.4	1.6	1.79	2.8×10^{10}	1.9	3.1	2.8
		.3	.53	.61	.27	5.4	↓	1.81	3.8	1.7	3.2	2.7
		.4	.57	.81	.27	5.4		1.90	5.2	1.7	3.2	2.7
		.5	.60	.95	.24	5.5		2.04	6.0	1.6	3.3	2.6
		.6	.62	1.1	.24	5.5		2.19	6.7	1.5	3.3	2.6
		.8	.66	1.5	.26	5.4		2.41	8.3	1.4	3.4	2.5
		1.0	.69	1.8	.23	5.5	↓	2.64	9.5	1.3	3.4	2.5
		1.5	.77	2.5	.22	5.6	1.5	2.98	11	.97	3.7	2.3
		2	.84	3.0	.20	5.7	1.5	3.21	12	.77	3.9	2.2
		3	.98	3.9	.17	6.0	1.4	3.47	10	.46	4.4	1.9
		4	1.17	4.5	.14	6.4	1.3	3.61	7.8	.26	5.2	1.6
		5	1.44	4.8	.13	6.6	1.3	3.70	4.3	.11	7.0	1.2

ate for the relative containment. The second comparison is illustrated in figure 32 and table III and represents equal net containment in the sense that the electrode currents were the same for the positive and negative polarities, but the electrode voltages were whatever was required to produce those equal currents.

In figures 31 and 32 the data denoted by the solid circular symbols on the lower lefts of the graphs were taken with positive electrode polarities, and the data denoted by the open circular symbols to the upper rights were taken with negative electrode polarities. All other conditions, including the electrode voltage in figure 31 and the total current in figure 32, were the same. The number densities and containment times were about a factor of 10 or more larger for the negative polarities than for the positive polarities when electrode voltages were equal. Figure 31 makes it quite clear that the direction of the radial electric field has a substantial effect on the density and containment time of the plasma.

The same type of data are shown in figure 32, except that the data points shown are for equal currents with positive and negative electrode polarities. The significant difference between the two polarities is also evident, with the number densities and containment times between factors of 5 and 10 larger for the negative polarities. It appears that negative midplane electrode polarities are much more conducive to plasma containment than positive electrode polarities, as we might expect from the argument that the ions are being pushed radially inward by the electric fields when the polarities are negative.

Comparison with Bohm Containment Time

The containment times reported in figures 31 and 32 are in many cases greater than 1 millisecond, and as high as 1.9 milliseconds under the nonoptimized conditions investigated in this report. It is anticipated that elimination of particle drift due to toroidicity of the electric field and radial misalinement of the electrode rings will further improve the electron number densities and plasma containment times. The containment times above 1 millisecond are nonetheless quite gratifying, especially since they have been observed in the presence of very strong radial electric fields, which might be expected to impair plasma containment. It is therefore of some interest to compare these observed containment times with a benchmark, that of Bohm diffusion.

Bohm diffusion is a very imprecise concept that has been discussed in many standard references (e.g., ref. 27). Reference 27 gives for the Bohm diffusion coefficient

$$D_{Bohm} = \frac{T_e}{16B} \quad m^2/sec \tag{11}$$

where the electron temperature is measured in electron volts and the magnetic field in teslas. The factor of 1/16 is empirical and was first suggested by Bohm. More careful recent measurements by Geissler (ref. 28) indicate that plasmas confined within conducting walls exhibit Bohm diffusion with a coefficient that is 2.2 times Bohm's value. This somewhat larger coefficient will be used in the present work. If the plasma has a diffusive Bessel function radial profile, the relation between the containment time and the diffusion coefficient is

$$\frac{1}{\tau_{Bohm}} = 2.2 D_{Bohm} \left(\frac{2.405}{r}\right)^2 \quad \text{sec}^{-1} \tag{12}$$

where r is the minor radius of the plasma. We can substitute equation (11) into equation (12), and the Bohm diffusion time is given by equation (13).

$$\tau_{Bohm} = 1.26 \frac{r^2 B}{T_e} \quad \text{sec} \tag{13}$$

In the bumpy-torus plasma, the plasma radius at the location of the microwave interferometer is 6.6 centimeters, and the magnetic field on the interferometer axis is 1.56 teslas at the standard magnetic field condition of $B_{max} = 2.4$ teslas. Substituting these into equation (13) yields an expression for the Bohm containment time,

$$\tau_{Bohm} = \frac{8.56}{T_e} \quad \text{msec} \tag{14}$$

where the containment time is in milliseconds and the electron temperature is in electron volts.

If this experiment were an ohmically heated Stellarator or Tokamak, the electron temperature would be at least 100 electron volts and the Bohm containment time would be no more than 86 microseconds. Examination of the experimental data in figures 31 and 32 shows that the containment times are, in general, much greater than 86 microseconds. Looked at in this way, the containment times achieved with positive electrode polarities are about the same as those that could have been achieved by an ohmically heated plasma of the same dimensions in the same magnetic field. And the containment times observed with negative midplane polarities are a factor of 10 or 20 higher than those that could have been achieved if this were an ohmically heated Stellarator or Tokamak.

It may be objected that this comparison is too hypothetical, and that we should substitute into equation (14) the electron temperature that actually exists in the bumpy-torus plasma. The data in figures 31 and 32 were not accompanied by diagnostic measurements of the electron temperature. Measurement of the electron temperature is extremely difficult, even by the helium line ratio technique reported previously for the bumpy torus in references 1, 16, and 20. However, there exists a means of estimating the electron temperature of the bumpy-torus plasma, since (as has been shown in refs. 16 and 20) the electron temperature can be inferred from the average particle containment time. The particle containment time can be set equal to the ionization time in equation (15):

$$\tau_i = \tau_p = \frac{1}{n_0 \langle \sigma v \rangle_{ne}} \tag{15}$$

in which n_0 is the background neutral number density and $\langle \sigma v \rangle_{ne}$ is the ionization rate coefficient, shown in figure 33, for the electron-impact ionization of deuterium gas. We can set the average particle containment time calculated from equation (2) equal to the ionization time in equation (15) and use the data in figure 33 (or extrapolations of it to

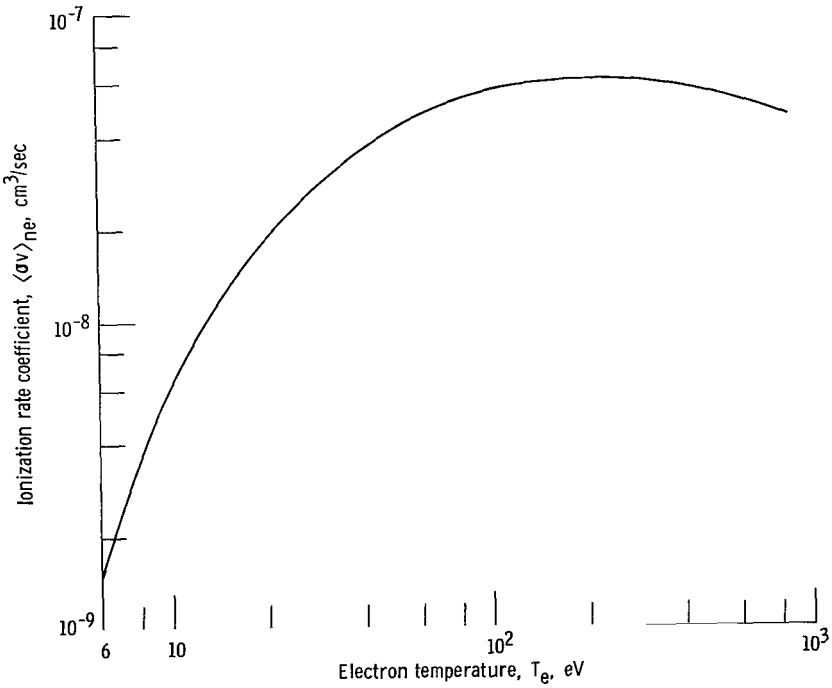

Figure 33. - Ionization rate coefficient for electron impact of deuterium, as function of electron temperature. ($e + D_2 \rightarrow D_2^+ + 2e.$)

lower electron temperatures) to estimate the electron temperature that must exist in order to provide a balance between ionization and loss in this steady-state plasma. This has been done, and the resulting electron temperatures, ranging from 3 to 10 electron volts, were used to calculate the Bohm containment times listed in tables II and III. These Bohm containment times are plotted as the triangular symbols in figures 31 and 32, with the open triangles representing negative polarities, and the solid triangles positive polarities. By comparing data of the same polarity, we can see that the Bohm containment times are about an order of magnitude higher than the observed data for positive polarities, but are within a factor of 2 of the containment times observed for negative polarities.

The Bohm containment data in figures 31 and 32 are encouraging because they imply that even the presence of very strong electric fields, which approach and probably exceed 1 kV/cm in the plasma, does not result in plasma containment times significantly shorter than the Bohm value when the radial electric fields point inward. The containment data reported in figures 31 and 32 are not yet optimized, and it is anticipated that higher densities and containment times will be achieved.

DISCUSSION AND CONCLUSIONS

A microwave interferometer operating on a polarization diplexing principle has been put into operation and can measure the number density of the plasma over a range from 10^8 to over 10^{11} particles/cm^3. Spectroscopic and other lines of investigation imply that the current drawn from the plasma is not ambipolar and that charges of opposite sign go to their respective electrodes. This is consistent with the imposition of strong electric fields on the plasma from an external power supply and is a characteristic feature of this approach to plasma heating and containment. It has been shown that any parasitic currents must be small, less than 1 percent of the total plasma power, and that any ambipolar currents which exist must be a fixed fraction of the total electrode current, over more than three orders of magnitude in the current. The absence of ambipolar current flows makes possible the direct calculation of the average particle and energy containment times according to expressions given in equations (2) and (4) of the text. The particle containment time requires a measurement only of the electrode current, the average electron number density in the plasma, and the plasma volume. A lower bound on the energy containment time can be calculated if the ion kinetic temperature and the electrode voltage are known in addition. The particle containment times calculated for the data taken in this report range up to 1.9 milliseconds: however, the operating conditions have not been optimized, nor has the apparatus been pushed to the limits of its operating range.

The plasma displays good toroidal symmetry, with equal currents drawn by the electrode rings in each of the 12 sectors when the neutral background gas is injected in a symmetric manner and when there are no leaks in the vacuum system. The electron number density in the low-pressure mode of operation does not vary significantly when a single midplane electrode ring is moved successively from one sector to another around the plasma, relative to the fixed position of the diagnostic apparatus. The method of neutral gas injection and the alinement of the midplane electrode ring both affect the symmetry of the plasma and/or its current-voltage curves.

Four impurity gases - helium, nitrogen, neon, and argon - were deliberately introduced into the plasma at increasing concentrations, and these impurities had no significant effect on either the ion kinetic temperature, measured with a charge-exchange neutral detector, or the electron number density, measured with the microwave interferometer. These results indicate that the small background impurities normally present in the plasma do not in any way affect the measurement of electron number density or ion kinetic temperature.

The effects of the plasma configuration and the number of electrode rings on the electron number density and the ion kinetic temperature are rather complex and are summarized in figures 21 and 22. For positive polarities, the number of electrode rings and their configuration do not significantly affect the average electron number density in the low-pressure mode of operation. However, in the high-pressure mode of operation the number density increases as the number of electrode rings is decreased even though the configuration does not affect the results. For negative electrode polarities the number density in the low-pressure mode of operation does not seem to be affected by either the configuration or the number of electrode rings. However, in the high-pressure mode of operation the electron number density is affected both by the configuration and the number of electrode rings used.

With positive polarity, there does not seem to be a systematic dependence of the ion kinetic temperature on the number of electrode rings or their polarity, with the possible exception of the low-pressure mode of operation. With negative electrode polarities in the low-pressure mode of operation, some data were taken in figure 22 which indicate that the ion kinetic temperature decreased as the number of electrodes was decreased.

A paired comparison study was made of the average electron number density and the particle containment time, with the same two electrodes generating the plasma and with the same background pressures, magnetic fields, alinements, and electrode voltages or currents. The electrode polarity was a significant variable. The containment times and number densities were an order of magnitude or more larger when the electric fields pointed radially inward than they were when the electric fields pointed outward.

The highest particle containment time observed thus far was 1.9 milliseconds; the highest average electron number density was 1.3×10^{11} particles/cm^3, which corresponds to a maximum density on the plasma axis of 2.7×10^{11} particles/cm^3. The highest fraction ionized was 18 percent. These data were taken under conditions in which the ion kinetic temperature would have been of the order of 200 or 300 electron volts. The highest ion kinetic temperature ever observed in this plasma has been 2500 electron volts for deuterium ions. These data were taken for unoptimized conditions, and it is anticipated that significantly higher values will be possible when the alinement and geometry of the electrode rings are optimized. The containment times have been achieved in the presence of electric fields that often exceed 1 kV/cm.

If we were to compare the bumpy-torus plasma with that of a Stellarator or Tokamak of similar magnetic field and radius, the Bohm containment times of such an equivalent experiment would be less than 0.10 millisecond, an order of magnitude below the containment times actually observed in the present experiment. If, however, we estimate the electron temperatures in this plasma and calculate the appropriate Bohm containment times, the best containment times that we observed so far (under nonoptimized conditions) are comparable to the calculated Bohm containment times. The present preliminary data quite clearly demonstrate an order-of-magnitude effect on plasma containment of the direction of the electric field and indicate that the ions are better contained when they are at the bottom of an electrostatic potential well in the toroidal plasma.

Lewis Research Center,
National Aeronautics and Space Administration,
Cleveland, Ohio, January 3, 1977,
506-25.

APPENDIX - SYMBOLS

A	area, m^2
B_{max}	maximum magnetic field on magnetic axis, T
D_{Bohm}	Bohm diffusion coefficient, m^2/sec
e	electronic charge
I_p	electrode current flowing to plasma, A
$\bar{n}_e$	average electron number density, particles/cm^3
$n_{e, max}$	maximum electron number density, particles/cm^3
n_0	neutral particle density in plasma, particles/cm^3
P_W	parasitic power, W
r	radius, m
t	time, sec
T_e	electron kinetic temperature, eV
T_i	ion kinetic temperature, eV
T_m	melting point of sheet metal, K
V_a	electrode voltage, V
V_p	plasma volume, m^3
W_p	electrical power input to plasma, W
W_{pa}	parasitic power flux, W/m^2
ϵ	emissivity
σ	Stefan-Boltzmann constant
$\langle \sigma v \rangle_{ne}$	electron neutral ionization rate coefficient, m^3/sec
τ_{Bohm}	Bohm diffusion time, sec
τ_c	average particle containment time, sec
τ_E	average energy containment time, sec
τ_i	ionization time, sec

REFERENCES

1. Roth, J. Reece; Gerdin, Glen A.; and Richardson, Richard W.: Characteristics of the NASA Lewis Bumpy-Torus Plasma Generated with Positive Applied Potentials. NASA TN D-8114, 1976.

2. Roth, J. Reece; Gerdin, Glen A.; and Richardson, Richard W.: Characteristics of NASA Lewis Bumpy Torus Plasma Generated with Positive Applied Potentials. IEEE Trans. Plasma Sci., vol. PS-4, no. 3, Sept. 1976, pp. 166-176.

3. Roth, J. Reece: Plasma Stability and the Bohr-Van Leeuwen Theorem. NASA TN D-3880, 1967.

4. Roth, J. Reece; et al.: A 12-Coil Superconducting 'Bumpy Torus' Magnet Facility for Plasma Research. Fifth Applied Superconductivity Conference. Inst. Electr. Electron. Eng., Inc., 1972, pp. 361-366.

5. Roth, J. R.; et al.: Performance of a 12-Coil Superconducting 'Bumpy Torus' Magnet Facility. Proc. Technology of Controlled Thermonuclear Fusion Experiments and the Engineering Aspects of Fusion Reactors. Am. Nucl. Soc., 1974, pp. 409-425.

6. Roth, J. Reece; et al.: Characteristics and Performance of a Superconducting Bumpy-Torus Magnet Facility for Plasma Research. NASA TN D-7353, 1973.

7. Roth, J. Reece: Experimental Study of Spectral Index, Mode Coupling, and Energy Cascading in a Turbulent, Hot-Ion Plasma. Phys. Fluids, vol. 14, no. 10, Oct. 1971, pp. 2193-2202.

8. Roth, J. Reece: Origin of Hot Ions Observed in a Modified Penning Discharge. Phys. Fluids, vol. 16, no. 2, Feb. 1973, pp. 231-236.

9. Roth, J. Reece: Hot Ion Production in a Modified Penning Discharge. IEEE Trans. Plasma Sci., vol. PS-1, no. 1, Mar. 1973, pp. 34-45.

10. Roth, J. R.: Energy Distribution Functions of Kilovolt Ions in a Modified Penning Discharge. Plasma Phys., vol. 15, no. 10, Oct. 1973, pp. 995-1005.

11. Roth, J. Reece; and Gerdin, Glenn A.: Characteristics of the NASA Lewis Bumpy-Torus Plasma Generated with High Positive or Negative Applied Potentials. NASA TN D-8211, 1976.

12. Roth, J. Reece: Preliminary Scaling Laws for Plasma Current, Ion Kinetic Temperature, and Plasma Number Density in the NASA Lewis Bumpy Torus Plasma. NASA TM X-73434, 1976.

13. Dandl, R. A.; et al.: Plasma Confinement and Heating in the ELMO Bumpy Torus (EBT). Proc. Fifth Int. Conf. on Plasma Physics and Controlled Nuclear Fusion Research. IAEA-CN-33/B6, Vol. II, Int. Atomic Energy Agency, 1974, pp. 141-149.

14. Dandl, R. A.; Dory, R. A.; and Eason, H. O.: Research Program for Plasma Confinement and Heating in ELMO Bumpy Torus Devices. ORNL TM-4941, Oak Ridge National Lab., 1975.

15. Thermonuclear Division, Annual Progress Report. ORNL-5154, Oak Ridge National Lab., 1976, pp. 5-12.

16. Richardson, Richard W.: Effect of Anode Ring Arrangement on the Spectroscopic Characteristics of the NASA Lewis Bumpy Torus Plasma. NASA TM X-71636, 1974.

17. Gardner, A. L.: A Microwave Diagnostics System - Immune to Thermal Expansion - for Use in a Steady State Plasma. Am. Phys. Soc. Bull., vol. 20, no. 10, Oct. 1975, p. 1322.

18. Gardner, A. L.: Microwave Instrumentation for Polarization Diplexing at 27 GHz. IEEE Plasma Science Conference. 76CH1083-5-NPS, 1976, p. 47.

19. Perkins, R. T.; and Gardner, A. L.: Interpreting the Plasma Phase Shift of a Polarization-Diplexing Microwave Interferometer. Am. Phys. Soc. Bull., vol. 21, no. 9, Oct. 1976, p. 1117.

20. Richardson, Richard W.: Spectroscopic Results in Helium Gas from the NASA Lewis Bumpy Torus Plasma. NASA TM X-71569, 1974.

21. Gray, Dwight E., ed.: American Institute of Physics Handbook. McGraw-Hill Book Co., Inc., 1957.

22. Weast, Robert C., ed.: Handbook of Chemistry and Physics. 45th ed., Chemical Rubber Publishing Co., 1964.

23. Valckx, F. P. G.: Electrostatic Analyzer for the Detection of Fast Neutral Particles. NASA TT F-11, 458, 1968.

24. Stirling, W. L.: Lifetime of Hot-Ion Plasma in a Mirror Machine. Phys. Fluids, vol. 15, no. 1, April 1972, pp. 688-692.

25. Reinmann, J. J.; et al.: Hot Ion Heating Experiments in SUMMA. IEEE Trans. Plasma Sci., vol. PS-3, no. 1, Mar. 1975, pp. 6-14.

26. Summers, Robert L.: Empirical Observations on the Sensitivity of Hot Cathode Ionization Type Vacuum Gages. NASA TN D-5285, 1969.

27. Glasstone, Samuel; and Lovberg, Ralph H.: Controlled Thermonuclear Reactions. D. Van Nostrand & Co., 1960, p. 462.

28. Geissler, K. H.: On the Influence of Boundary Conditions on the Diffusion of a Weakly Ionized Plasma Across a Magnetic Field. Plasma Phys., vol. 10, 1968, pp. 127-136.

"The aeronautical and space activities of the United States shall be conducted so as to contribute . . . to the expansion of human knowledge of phenomena in the atmosphere and space. The Administration shall provide for the widest practicable and appropriate dissemination of information concerning its activities and the results thereof."

—NATIONAL AERONAUTICS AND SPACE ACT OF 1958

NASA SCIENTIFIC AND TECHNICAL PUBLICATIONS

TECHNICAL REPORTS: Scientific and technical information considered important, complete, and a lasting contribution to existing knowledge.

TECHNICAL NOTES: Information less broad in scope but nevertheless of importance as a contribution to existing knowledge.

TECHNICAL MEMORANDUMS: Information receiving limited distribution because of preliminary data, security classification, or other reasons. Also includes conference proceedings with either limited or unlimited distribution.

CONTRACTOR REPORTS: Scientific and technical information generated under a NASA contract or grant and considered an important contribution to existing knowledge.

TECHNICAL TRANSLATIONS: Information published in a foreign language considered to merit NASA distribution in English.

SPECIAL PUBLICATIONS: Information derived from or of value to NASA activities. Publications include final reports of major projects, monographs, data compilations, handbooks, sourcebooks, and special bibliographies.

TECHNOLOGY UTILIZATION PUBLICATIONS: Information on technology used by NASA that may be of particular interest in commercial and other non-aerospace applications. Publications include Tech Briefs, Technology Utilization Reports and Technology Surveys.

Details on the availability of these publications may be obtained from:

SCIENTIFIC AND TECHNICAL INFORMATION OFFICE

NATIONAL AERONAUTICS AND SPACE ADMINISTRATION

Washington, D.C. 20546